crystals

MDPI

Review

Cation Doping Approach for Nanotubular Hydrosilicates Curvature Control and Related Applications

Andrei A. Krasilin [1,*], Ekaterina K. Khrapova [1] and Tatiana P. Maslennikova [1,2]

1 Ioffe Institute, St. Petersburg 194021, Russia; e.k.khrapova@mail.ioffe.ru (E.K.K.); maslennikova.tp@iscras.ru (T.P.M.)
2 Grebenshchikov Institute of Silicate Chemistry of the RAS, St. Petersburg 199034, Russia
* Correspondence: ikrasilin@mail.ioffe.ru

Received: 29 June 2020; Accepted: 29 July 2020; Published: 30 July 2020

Abstract: The past two decades have been marked by an increased interest in the synthesis and the properties of geoinspired hydrosilicate nanoscrolls and nanotubes. The present review considers three main representatives of this group: halloysite, imogolite and chrysotile. These hydrosilicates have the ability of spontaneous curling (scrolling) due to a number of crystal structure features, including the size and chemical composition differences between the sheets, (or the void in the gibbsite sheet and SiO_2 tetrahedron, in the case of imogolite). Mineral nanoscrolls and nanotubes consist of the most abundant elements, like magnesium, aluminium and silicon, accompanied by uncontrollable amounts of impurities (other elements and phases), which hinder their high technology applications. The development of a synthetic approach makes it possible to not only to overcome the purity issues, but also to enhance the chemical composition of the nanotubular particles by controllable cation doping. The first part of the review covers some principles of the cation doping approach and proposes joint criteria for the semiquantitative prediction of morphological changes that occur. The second part focuses on some doping-related properties and applications, such as morphological control, uptake and release, magnetic and mechanical properties, and catalysis.

Keywords: chrysotile; halloysite; imogolite; nanotubes; nanoscrolls; modelling; hydrothermal synthesis; composite materials; catalysis

1. Introduction

The year 2020 can be considered as the 90th anniversary of inorganic nanotubes. In 1930, L. Pauling [1] assumed the ability of certain hydrosilicate layers to curve because of size differences between alternating sheets. Following the development of electron microscopes, the tubular morphology of halloysite and chrysotile minerals was successfully visualised in 1949–1950 [2–4]. In the next decades, the geoinspired synthetic experiments, X-ray diffraction and microscopic studies of R. Roy and D.M. Roy [5], J.C.-S. Yang [6], H. Saito and I. Yamai [7,8], K. Yada and K. Iishi [9], and E.J.W. Whittaker [10–13] contributed greatly to hydrosilicate nanotubes' classification and the understanding of their growth mechanism. The third nanotubular mineral that will be considered in this review was discovered and synthesised a little later [14–16]. Revealing imogolite's tubular morphology was more challenging than with chrysotile and halloysite because of the substantially smaller size of the former. Despite such a long history of the study of tubular hydrosilicate particles, the famous term 'nanotube' only appeared after the carbon nanotubes' observations made by S. Iijima [17], and this was related, perhaps, to the remarkable progress that had been made in electronic component miniaturisation.

The aim of the present review was, first, to look at chrysotile, halloysite and imogolite as related hydrosilicates, whose formation process, growth, and specific morphology obey similar rules.

For example, the hydrothermal synthesis of halloysite nanotubes is still very complicated and most published papers have used halloysite mineral for a variety of applications. It might be argued that the mineral is available in large amounts, but this does not excuse the lack of synthetic results. We believe that a comparative study of the related hydrosilicates will help to reveal, and probably overcome, that hindrance.

Second, pristine chrysotile, halloysite and imogolite nanotubes contain Mg, Al and Si cations, which can be substituted by other elements during a synthetic experiment. We hope that the joint consideration of the three hydrosilicates will promote an exchange of ideas and approaches to their synthesis. Moreover, since the cation type and content are among the key factors of morphology control, it is important to reveal regularities and possible limitations of cation doping of the hydrosilicate layer.

Third, a general aim of cation doping is to confer a new property on the hydrosilicate nanotube, so this should be discussed as well.

In accordance with these aims, the present review consists of three sections, in addition to the Introduction and Conclusion. Section 2 is devoted to an overview of hydrosilicates' structural modelling and the contemporary principles of the cation doping approach. Section 3 considers synthesis and some cation doping-related morphological effects. Section 4 reviews a number of properties and applications of cation doped hydrosilicate nanotubes and nanoscrolls. We will use both the term 'nanotube' and 'nanoscroll', because both forms of cross-section can be observed for hydrosilicates. 'Nanoscroll' is more appropriate when a is model based on a spiral form, or when a formation mechanism via scrolling, is considered.

2. Principles of Curvature Control

2.1. Crystal Structure and the Origin of Strain

The crystal structures of chrysotile, halloysite and imogolite are wrapped around the very similar idea of the joining of two different polyhedral motives or sheets. In the case of chrysotile, these sheets are brucite-like octahedrons and a pseudohexagonal network of silica tetrahedrons (Figure 1). A gibbsite-like octahedral sheet constitutes halloysite (Figure 2) and imogolite (Figure 3) layers. The latter has silica tetrahedrons separated from one another. At first glance, it would seem that structural variations in those hydrosilicates are insignificant, but they suddenly lead to striking differences in morphology. First, it is the direction of the layer's bending: chrysotile and imogolite curve in such a manner that the octahedral sheet becomes the outer one, while in the case of halloysite, this sheet becomes the inner one. Moreover, only imogolite tends to form single-walled nanotubes, whereas chrysotile and halloysite are multi-walled, and sometimes this wall consists of tens of layers. Adjacent layers are directly joined together by hydrogen bonding, but sometimes, in halloysite there is an additional buffer layer of water molecules situated in between (Figure 2) that increases the interlayer period. This structural modification is called 10 Å-halloysite, whereas its dehydrated version (with a period similar to chrysotile) is called 7 Å-halloysite [18]. It is intriguing that reports on a possibly hydrated version of chrysotile are absent. The morphological diversity of those three hydrosilicates goes beyond tubular morphology. To date, platy lizardite [19] and kaolinite [20] are known to be platy analogues of chrysotile and halloysite. Spherical allophane [21,22] and polyhedral endellite [23,24] could form instead from tubular imogolite and halloysite, whereas chrysotile has its polygonal variation [25–27].

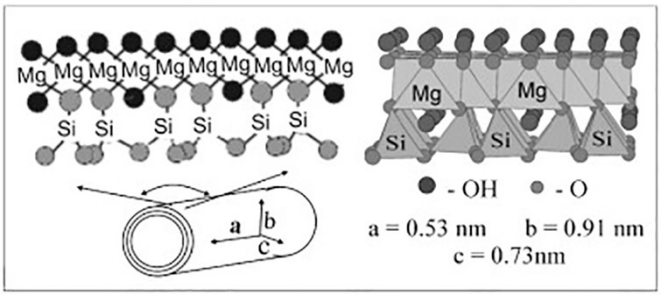

Figure 1. The schematic crystalline structure of chrysotile. From [28]. Copyright ©2011 Elsevier Ltd., Amsterdam, The Netherlands.

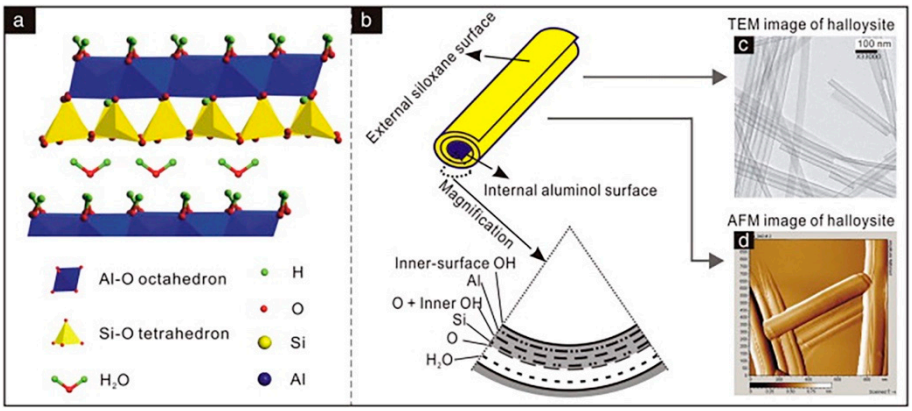

Figure 2. Schematic diagram of (**a**) the crystalline structure of 10 Å-halloysite, (**b**) the structure of a halloysite particle, and (**c**,**d**) the transmission electron microscope and atomic force microscope (AFM) images of halloysite. From [18]. Copyright ©2015 Elsevier Ltd., Amsterdam, The Netherlands.

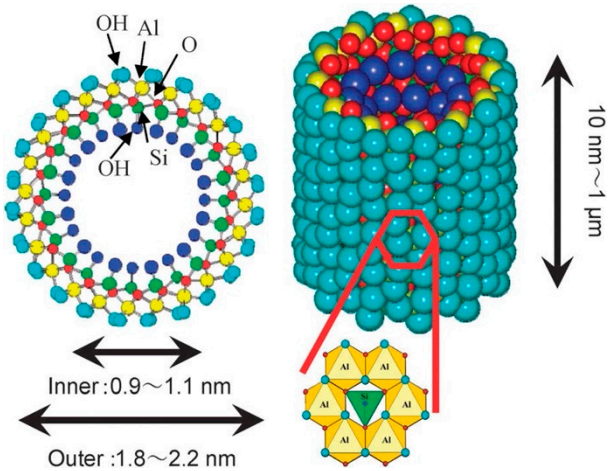

Figure 3. Structural illustration of imogolite, synthesised in [29]. Reproduced with permission from the Centre National de la Recherche Scientifique (CNRS), Paris, France, and The Royal Society of Chemistry, Cambridge, United Kingdom.

According to recent structural studies, chrysotile is a monoclinic *Cc* space group with lattice constants $a = 0.5340(1)$ nm, $b = 0.9241(1)$ nm and $c = 1.4689(2)$ nm, $\beta = 93.66(3)°$ [30]. Its cell consists of two layers in the c direction. Zhang et al. [31] assigned triclinic *P1* group to 7 Å-halloysite with lattice constants $a = 0.51616(6)$ nm, $b = 0.88304(10)$ nm and $c = 0.75032(8)$ nm (one layer in the cell), $\alpha = 93.992(12)°$, $\beta = 104.526(12)°$ and $\gamma = 89.661(10)°$. All of these values were obtained by crystal structure refinement using wide-angle X-ray scattering. Demichelis et al. [32] proposed to use the gibbsite ($a = 0.511$ nm, $b = 0.876$ nm, $\gamma = 88.8°$) cell as an initial approximation for

imogolite for ab initio calculations. An interpretation of X-ray patterns in the case of imogolite involved the supercells of nanotube aggregates [33,34]. Alvarez-Ramírez [34] also attempted to optimise a hypothetical flat imogolite unit cell using the Density Functional Theory (DFT) approach and revealed that the parameters $a = 0.49$ nm and $b = 0.846$ nm were less than that of gibbsite.

In order to reveal the origin of strain and curvature in those hydrosilicates, the initial structures of the sheets should be compared prior their chemical bonding. Figure 4 shows principal hydrosilicate building blocks. An estimation of the average cavity size in the $Al(OH)_3$ layer [35] as the distance between oxygen ions that would be shared between octahedra and tetrahedra yielded a value of 0.322 nm. The same procedure carried out for SiO_2 cristobalite tetrahedra [36] resulted in a value of 0.262 nm. The pseudohexagonal network of SiO_2 tetrahedra constructed on that basis would have a specific size of 0.907 nm. A comparison of these values with the specific sizes of $Mg(OH)_2$ (0.944 nm [37]) and $Al(OH)_3$ (0.864 nm) would lead to the conclusion that there is a substantial size difference between the structural elements which has to be overcome somehow. Moreover, this basic comparison enables the prediction of the main direction of scrolling, assuming that it is a means of size difference compensation.

The main principle of curvature control by cation doping relies on the idea that substitution will change the specific size of polyhedrons (sheets) and in turn, the preferred curvature of the layer.

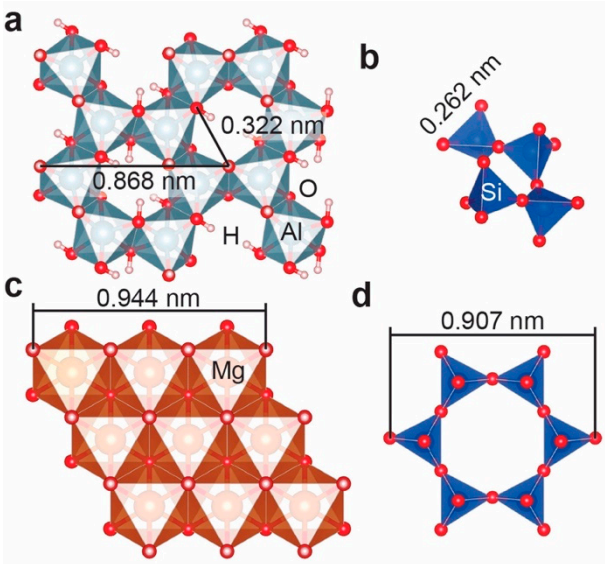

Figure 4. (**a**) Crystal structure of $Al(OH)_3$ gibbsite according to the data of Saalfeld and Wedde [35]. An averaged size of the cavity is shown. (**b**) Crystal structure of the SiO_2 cristobalite according to the data in [36]. An averaged size of the tetrahedra's side is shown. (**c**) Crystal structure and specific size of $Mg(OH)_2$ brucite reported in [37]. (**d**) An 'ideal' silica sheet adopted from the structural data in [38]. Specific size was calculated on the basis of the (**b**) value. VESTA software was used for visualisation [39].

2.2. *An Overview of Nanotube Modelling*

Although tubular particles were visualised by a transmission electron microscope in 1949–1950 [4], nanotube modelling advanced greatly after the observation of carbon nanotubes [17] and the discovery of their mechanical, electronic and morphological properties. This section considers two groups of models, divided by the principle of continuity. The first group includes the DFT and molecular dynamics (MD) approaches, which rely on precise nanotube crystal structure optimisation. Conversely, the second group of phenomenological modelling considers the layer as a continuous medium with a number of parameters and applies the equations obtained for macroscopic processes at the nanoscale or operates with time-dependent kinetic equations. Both groups have their strengths and weaknesses,

which will be highlighted below. We also recommend the book section, written by A. Enyashin [40], that considers recent advances in the modelling of inorganic nanotubes.

2.2.1. DFT and MD 'Microscopic' Models

We would like to start with an overview of the modelling of imogolite as the smallest nanotube. Its small size has facilitated computations, there being no need to involve large cells in order to achieve good agreement with the experiment. Early works that involved DFT and MD approaches were focused on preferable cross-section geometry. Konduri et al. [41] reported a single-walled imogolite nanotube diameter of 1.98 nm based on aluminium atoms and an outer diameter of 2.26 nm, whereas experimental evidence suggested that this should be 2.2 nm. The authors also calculated the dependence of radial breathing mode frequency, which could be useful for the spectroscopic characterisation of imogolite. The work [34] considered the band gap X-ray scattering and vibrational frequency evolution in $(OH)_3Al_2O_3(Si_xGe_{1-x})OH$ imogolite nanoscrolls. The author demonstrated that Si to Ge substitution decreased the band gap value in a number of wave vector points (Figure 5). X-ray diffraction simulations revealed that the pattern depended more on the model nanotube radius than on the Si content. Guimarães et al. [42] adopted the concept of the chirality vector to study structure optimisation and the electronic and mechanical properties of zigzag- and armchair-type imogolites. The authors reported a substantial zigzag imogolite strain energy preference. The preferred curvature radius of 1 nm was in good correlation with results reported in [41]. The estimated Young's modulus of zigzag imogolite of different radii varied from 175 to 479 GPa. The calculations yielded a very high band gap value of 10 eV for imogolite. The work of Demichelis et al. [32] and Lee et al. [43] was focused on the role of hydroxyl groups in imogolite shaping. The authors showed that the energy difference between the two chirality types could be explained by the energy preference in the hydrogen bond network arrangement on imogolite surfaces (Figure 6). The proper orientation of hydrogen bonds could provide an additional 2.0 kJ/mol of preference per formula unit of zigzag imogolite. Moreover, Lee et al. [43] obtained the preferable imogolite diameter of 1.7 nm (zigzag nanotubes), which was a bit smaller than those reported in [32,41,42]. Perhaps, the hydrogen bond network can not only favour zigzag-imogolite formation, but bend the layer in addition to the action of size difference between the sheets.

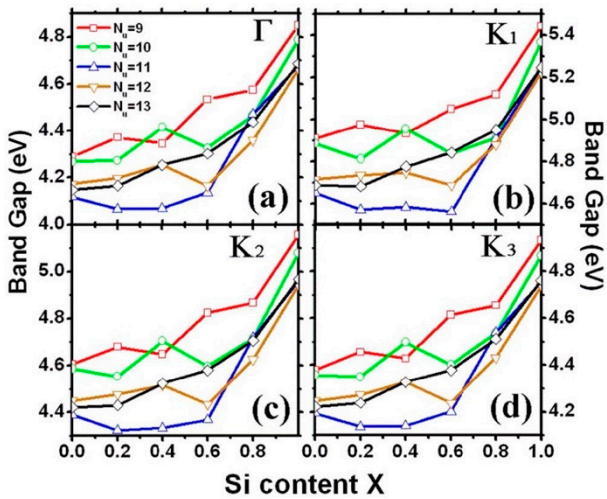

Figure 5. Band gap evolution for (**a**) Γ, (**b**) K_1, (**c**) K_2, and (**d**) K_3 points used in the calculation as a function of the radial dimension of the imogolite tubes. At the Γ(0,0,0) point, the band gaps have their minimum value, increasing with the content of silicon. The same behaviour with silicon content is observed at the other *k* points. From [34]. Copyright ©2007 American Physical Society, College Park, Maryland, United States.

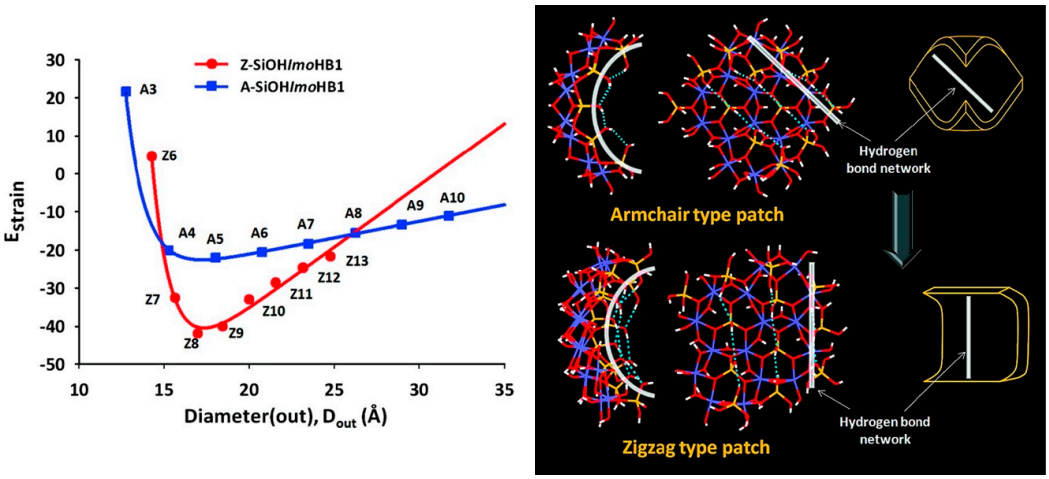

(**a**) (**b**)

Figure 6. (**a**) Calculated strain energies as a function of the outer diameter for zigzag (red circles) and armchair imogolite (blue squares). (**b**) Structural relaxation of a hydrogen terminated curved gibbsite-like imogolite patch. From [43]. Copyright ©2011 American Chemical Society, Washington, United States.

Some papers have been devoted to the study of substituted variations of imogolite. Alvarez-Ramírez [44] carried out a study of a general $(OH)_3N_2O_3MOH$ imogolite-like nanotube where M = C, Si, Ge, Sn and N = Al, Ga, In. The author demonstrated a change in the preferable cross-section geometry from a circular one to an elliptical and squared one with a more or less equal preferable radius expressed as a number of gibbsite-like units. In addition, the paper reported on a decrease in the direct band gap from around 4.7 eV to 2.5 eV with an0 increase in the M and N atomic numbers. The study [45] considered phosphorus and arsenic as potential substitutes for silicon. The authors demonstrated that changing Si increased the nanotube's preferable radius of curvature, but at the same time it decreased the energy effect of bending (Figure 7).

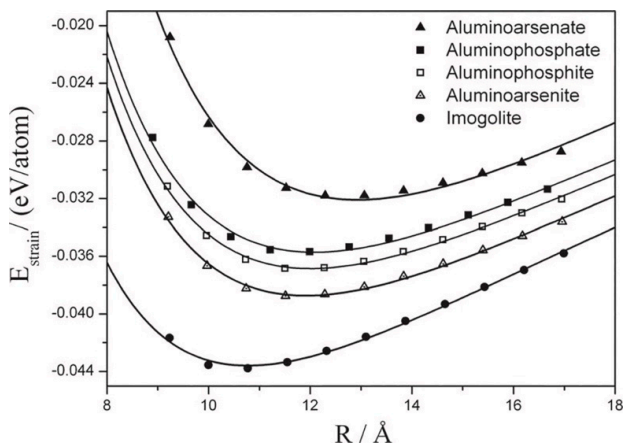

Figure 7. Strain energy per atom as a function of the tube radius of the (9,0)–(19,0) zigzag nanotubes aluminoarsenate (closed triangle), aluminophosphate (closed square), aluminophosphite (open square), aluminoarsenate (open triangle) and aluminosilicate imogolite (closed circle). From [45] with permission from the PCCP Owner Societies.

Another group of models has focused on the dynamics of imogolite layer scrolling. Using the MD approach, González et al. [46] revealed a high level of diversity in the manner of scrolling (Figure 8), including single, double and highly disordered spirals. An important result was that, in some cases, one complex spiral could be energy comparable to a system of two separate imogolite nanotubes.

Perhaps this was caused by the interaction between adjacent layers, which is interpreted as adhesion by some phenomenological models of scrolling. A generalised model of graphite, MoS_2 and imogolite layer bending was proposed in [47]. According to that research, a short imogolite layer, whose length was not enough to form a tube, gained almost the same curvature as the optimised tubes from previous studies (Figure 9). Thill et al. [22] extended the case of small imogolite layer bending in two possible directions in order to study the formation of spherical allophane. The authors demonstrated that the growing layer curved in both directions, forming the sphere's segment below a certain size threshold (Figure 10). Above this threshold, a sudden drop in curvature occurred, indicating the transition to a tubular growth regime. A probable allophane formation mechanism could be the self-organisation of a number of the sphere's segments by a kind of oriented attachment. According to [21], individual allophane particles usually were 4–5 nm in diameter, which might be formed of 6–9 sphere segments, 3 nm in size. Perhaps the resulting morphology (sphere or tube) could be a matter of kinetic competition between oriented attachment and recrystallisation, or between different modes of oriented attachment (attachment to edge or side surfaces of proto-imogolites).

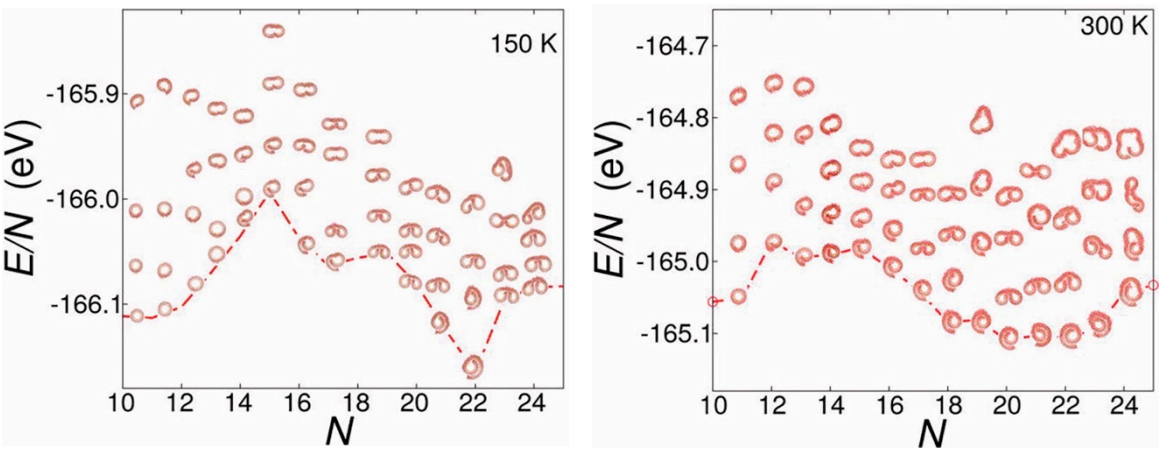

(**a**) (**b**)

Figure 8. Families of imogolite's cross-sections' conformations and their energies, obtained using planar initial conditions; (**a**) at 150 K; (**b**) at 300 K. N is a number of circular sectors, or unit cells. The red dashed line indicates the lowest energies for the various structures. From [46]. Copyright ©2014 American Chemical Society, Washington, United States.

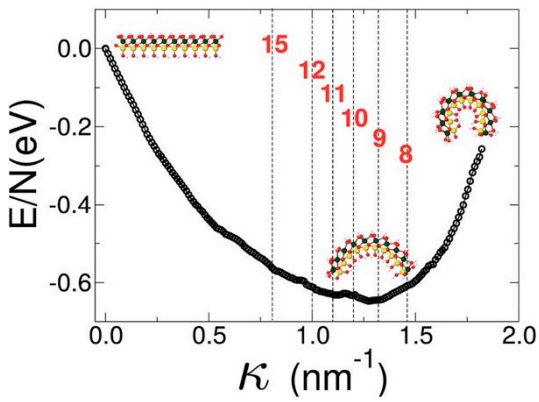

Figure 9. Energy vs. curvature of an imogolite sheet. The imogolite structure inset corresponds to $N = 5$ angular repetitions. The dashed vertical lines, and the numbers that label them, correspond to the curvature radius of a completely closed nanotube with that N value. Green Al; red O; yellow Si and light grey H. From [47] with permission from The Royal Society of Chemistry, Cambridge, United Kingdom.

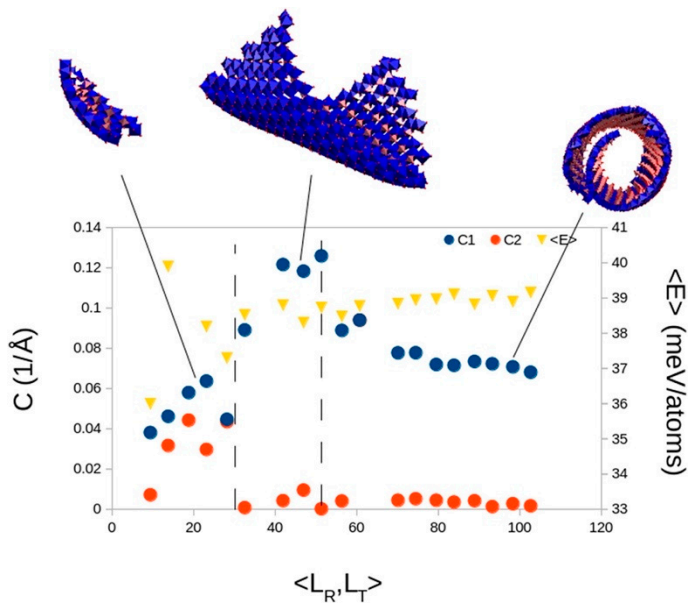

Figure 10. Average curvature and average stretching energy for planar initial conditions of increasing size from 5 to 100 Å. From [22]. Copyright ©2017 Elsevier B.V., Amsterdam, The Netherlands.

Finally, there are a number of theoretical papers with an accent on the mechanical and optical [48,49] properties of imogolite. The series of papers by D.Y. Kang et al. [50,51] relate to the classification of proposed models, because they combine DFT structure optimisation with Nanoscale Continuum Mechanics (NCM) for simulated mechanical tests. The authors revealed a dependence of the Young's and the share moduli on the single-walled imogolite nanotube's length during tensile, bending (Figure 11) and torsion loads. On the other hand, the presence of defects decreased both the Young's (340 GPa) and the shear (160 GPa) moduli of the tube. Liu and Kang [52] considered the mechanics of double-walled Ge-imogolite, highlighting the important role of the hydrogen bonds' interaction between the adjacent layers. Unfortunately, single- and double-layered cases were not compared, and this would have been of great value for the interpretation of diameter (number of layers) dependence of the Young's modulus observed in some nanomechanical experiments [53,54]. The pure MD simulation of imogolite nanotube compression was carried out in [55]. During the model experiment, the nanotube exhibited linear deformation with the Young's modulus around 200 GPa, then it lost stability and kinked in several places after reaching a critical curvature radius of around 100 nm.

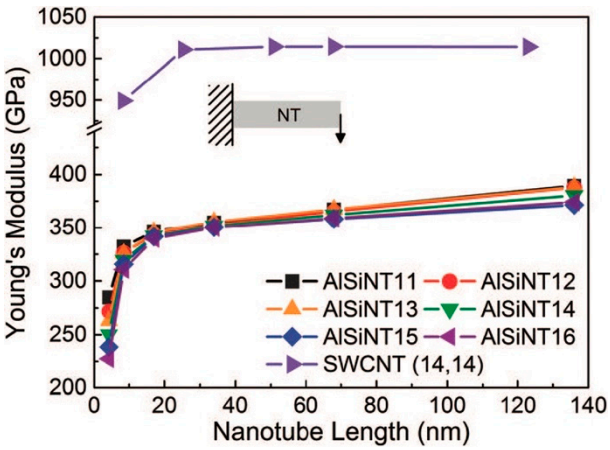

Figure 11. The Young's modulus of imogolite nanotubes of 11–16 unit cells, and single-walled (14,14) carbon nanotube as a function of nanotube length deduced from the simulated bending tests. From [50] with permission from The Royal Society of Chemistry, Cambridge, United Kingdom.

The number of theoretical papers that consider halloysite and chrysotile is relatively small. The structural, electronic and mechanical properties of single-walled halloysite and chrysotile were considered in [56,57]. The first issue identified for both hydrosilicates was that the cell size typical for imogolite was not enough to reach the energy minimum. The authors of [56,57] fitted the calculations with an empirical equation (Figure 12):

$$E_{\mathrm{str}} = \frac{a}{R^2} + \frac{b}{R} \tag{1}$$

taking into account the strain and surface energy differences in the form of the parameters a and b. Solving that equation relative to the energy minimum with specified parameters for halloysite and chrysotile returned radii of 3.3 nm and 11.2 nm (absolute values), respectively. The latter was overestimated in comparison to the work of Whittaker [13], who obtained the stress-free radius of 8.8 nm on the basis of X-ray pattern analysis. As for Young's modulus, the calculations yielded a value of around 300 GPa, which was comparable with imogolite. A recent large-scale DFT simulation of single-walled chrysotile [58] and other serpentine layers obtained the preferred radius of 8.8 nm (Figure 13), and this was in perfect agreement with [13].

The optimisation of 7 Å- and 10 Å-halloysite spirals, which accounted for no more than two layers (wraps), was carried out in [59]. One of the important results of this paper was a small distortion of the layer polyhedrons that was distributed across the entire supercell. Comparing two directions of scrolling, the authors revealed an energy preference of bending around the b axis due to the configuration of the hydrogen bond network. The scrolling of a flat halloysite layer was studied by means of the MD approach [60]. The authors revealed that scrolling occurred in both a and b crystallographic directions, but at a different speed. Intriguingly, the final inner radius of 5–15 nm significantly exceeded the value of 3.3 nm obtained by fitting the calculations of Guimarães et al. [56].

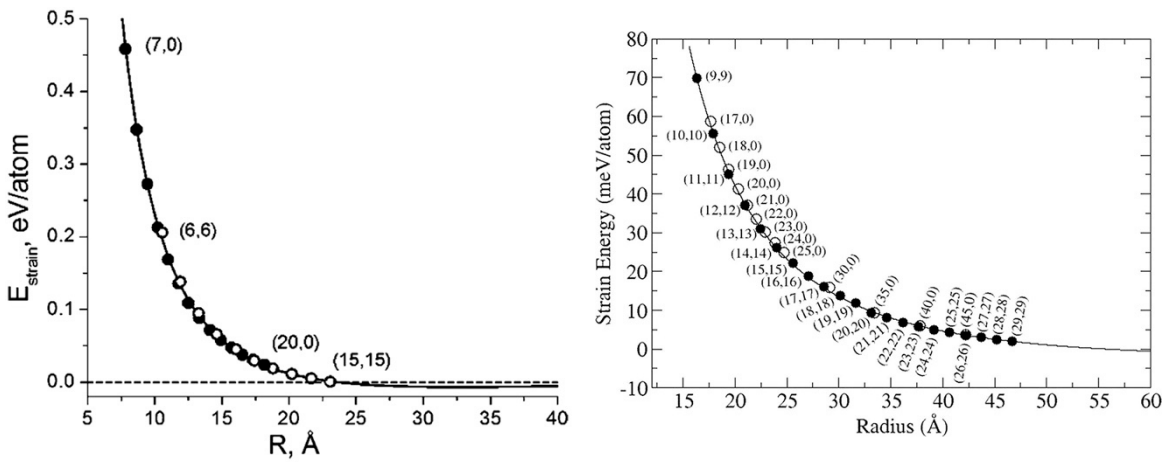

(**a**) (**b**)

Figure 12. (**a**) Strain energy as a function of the tube radius of (n,0) (closed circles) and (n,n) (open circles) single-walled halloysite nanotubes. Results are shown for the (7,0)–(20,0) and (6,6)–(15,15) nanotubes, from [56]. Copyright ©2010 American Chemical Society, Washington, United States. (**b**) Strain energy per atom as a function of the tube radius of the (17,0)−(45,0) zigzag (open circles) and the (9,9)−(29,29) armchair chrysotile nanotubes (closed circles), from [57]. Copyright ©2012 American Chemical Society, Washington, United States.

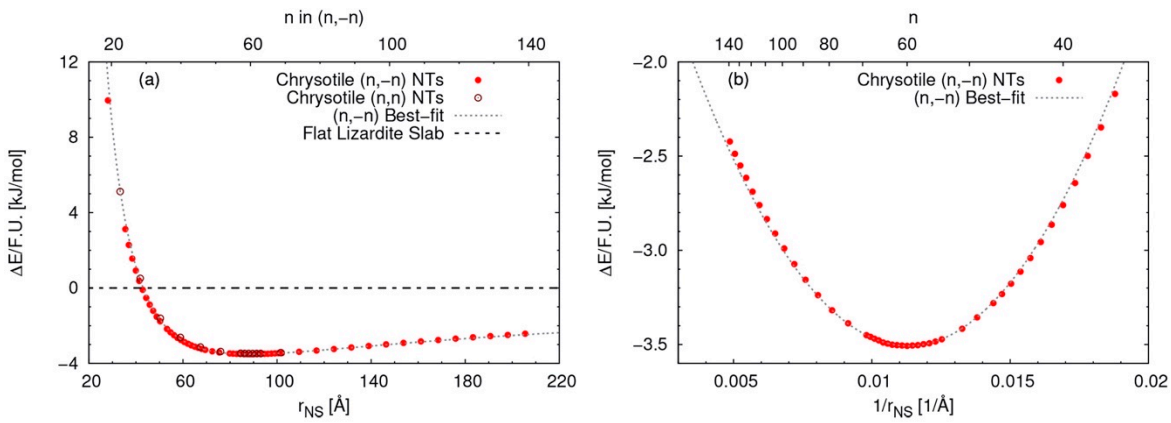

Figure 13. Energy difference per formula unit of (n; $-n$) single-walled chrysotile nanotubes with respect to the flat lizardite slab (kJ/mol), as a function of (**a**) the nanotube radius (Å) and index n, and (**b**) inverse nanotube radius (Å^{-1}) and index n. The superimposed curve was obtained using a quadratic best-fit over a set of 16 points around the energy minimum. From [58] with permission from The Royal Society of Chemistry, Cambridge, United Kingdom.

Very few papers have focused on the substituted versions of halloysite and chrysotile. Alvarez-Ramírez et al. [61] carried out a DFT structure optimisation of $Ni_3Si_2O_5(OH)_4$ nanoscrolls and demonstrated that the lattice constants were close to the $Mg_3Si_2O_5(OH)_4$, except they operated with a $P31m$ space group. Fu and Yang [62] considered the cation doping of kaolinite layers with Cr, Mn, Fe and Co, regardless of its scrolling ability. Cation doping initiated the cell volume expansion (except the Co substitution) and tuned the band gap of the layer. In addition, different cations preferred an anti- or ferromagnetic state.

2.2.2. Phenomenological 'Macroscopic' Models

In contrast to the group considered above, 'macroscopic' models consider the layer as, generally, a continuous medium, and attempt to describe scrolling using the analytical equations of mechanics and both thermo- and hydrodynamics. Some early papers considered probable ways of size difference compensation in a 1:1 hydrosilicate layer. Singh [63] compared the mechanism of tetrahedra rotation with whole layer rolling. The author came to the conclusion that the rotation mechanism might be less energy efficient due to the increasing Coulomb repulsion of the nearest Si atoms. In support of this conclusion, it seems that while the tetrahedral sheet distortion would decrease the size difference in one direction, it would simultaneously increase the difference in the other direction. However, the tetrahedral rotation mechanism could encourage nanotube form stabilisation after the scrolling, as the hydrogen bonds arrangement did.

One of the first studies of the energy aspects of substitutions was reported in [64]. The authors described the morphological transition of $Ni_3(Si_{1-x}Ge_x)_2O_5(OH)_4$ from tubes to plates in terms of the elastic theory of thin plates. A notable outcome of this research was the estimation of the preferred radius of curvature of $Ni_3Si_2O_5(OH)_4$ to be 9.13 nm, as well as the 1.068 J/m^2 surface stress difference between the opposite sides of the layer. In addition, using the concept of the size difference between the two sheets driven by an ionic radius of the cations, the authors estimated the molar fraction of Ge needed to eliminate the size difference to be $x = 0.3$. This value was well correlated with the synthetic experiment, which yielded $x = 0.25$. An energy model explaining the nanotubes' curvature was further developed in [65,66]. The authors considered the case of Si to Ge substitutions in imogolite,

accompanied by the formation of double-walled nanotubes and multi-walled nanoscrolls. The authors enhanced Equation (1) with the adhesion term in order to describe the multi-walled morphology:

$$\mathrm{E} = \frac{Yh^3}{3pR}\sum_{i=1}^{p}\frac{1}{R_i} - \frac{(\sigma_{\mathrm{int}} - \sigma_{\mathrm{ext}})h}{R} + \Sigma - \frac{p-1}{p}U \tag{2}$$

where Y is Young's modulus, h is a half of the layer's thickness, R is the mean radius of the ensemble, p is the number of layers, R_i is the curvature radius of the i layer, σ_{int} and σ_{ext} are the surface tension of the internal and external imogolite surfaces, $\Sigma = \sigma_{\mathrm{int}} + \sigma_{\mathrm{ext}}$ is total surface tension and U is the adhesion energy. Numerical calculation on the basis of this formula demonstrated the increased energy preference of multi-walled nanotubes and nanoscrolls with an increase in Ge content (Figure 14). In addition, an analytical approximation of this equation allowed authors to draw a sort of phase diagram (Figure 15) that described the competition between adhesion-associated (n_0) and strain/surface-associated (α) parameters for a wide range of nanotubular materials.

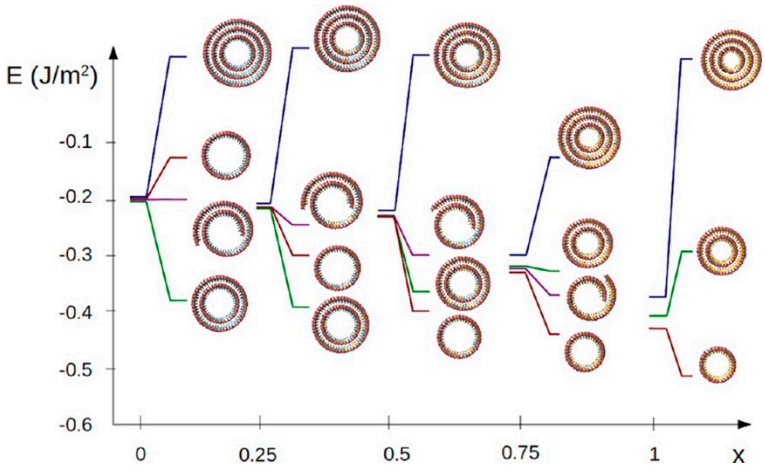

Figure 14. Energies of the $(OH)_3Al_2O_3Si_xGe_{1-x}(OH)$ shapes for x = 0, 0.25, 0.5, 0.75 and 1. The lowest-energy shape changes from double walled up to x = 0.25 to single walled. The energies are given considering Σ = 0. From [65]. Copyright ©2012 American Chemical Society, Washington, United States.

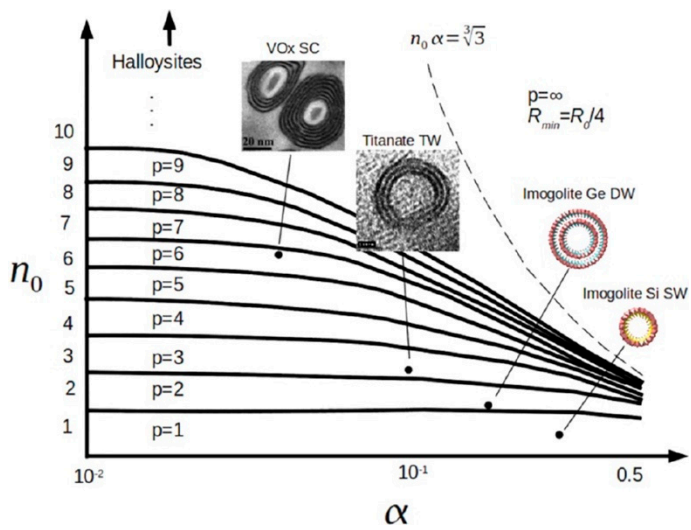

Figure 15. Minimum-energy diagram of multi-walled nanotubes and nanoscrolls as a function of dimensionless parameters. The positions of Si-imogolite, Ge-imogolite, titanate nanotubes and VO_x nanotubes are shown as examples, from [65]. Copyright ©2012 American Chemical Society, Washington, United States.

A group of phenomenological models used different time-dependent expressions in order to describe the scrolling process or nanotube growth. Chivilikhin et al. [67] studied the exfoliation and scrolling process of a chrysotile layer using a hybrid MD and continuous model. This approach made it possible to demonstrate the dynamics of the scrolling process once a part of the layer has been detached from the adjacent flat layer, and this is typical of a number of exfoliation processes. Depending on the allowances for spiral slip during the scrolling, the inner radius of the scroll remained constant or decreased continuously during the scrolling (Figure 16a) in order to compensate for the stress gain in the outer layers. According to the model, scrolling in a viscous liquid was quite a fast process that took tens of milliseconds. Later, the model was expanded to the case of nanoscrolls' ensemble [68] in order to track down the evolution of radius distribution (Figure 16b). The authors showed that, during recrystallisation, the nanoscrolls tried to reach some model equilibrium radius R_0.

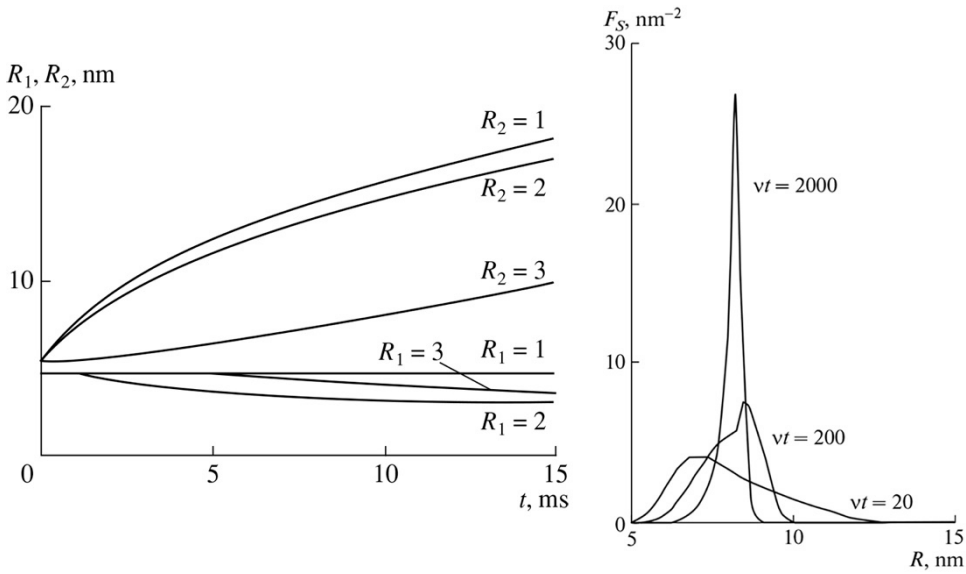

(**a**) (**b**)

Figure 16. (**a**) Dependences of the inner (R_1) and outer (R_2) radii of the nanoscroll on twisting time (1) without regard for the mutual slip of the coils, and with the inclusion of the mutual slip of the coils equal to (2) 0 and (3) 0.5, from [67]. Copyright ©2007 Pleiades Publishing, Ltd. (**b**) Evolution of the density distribution of the nanotube radius for the dimensionless time values vt, from [68]. Copyright ©2009 Pleiades Publishing Ltd., New York, United States.

While nanoscrolls' growth in diameter ('radial' growth) required additional model amendments in order to account for strain, it seems that the growth in length ('axial' growth) obeyed some conventional kinetics. Maillet et al. [69] compared the influence of dissolution (recrystallisation) and tip–tip collision, (it might also be called 'oriented attachment'), on the Ge-imogolite nanotubes' length distribution. Both hypotheses yielded theoretical length distribution curves that described experimental results fairly well (Figure 17) for long tubes. However, the model based on recrystallisation drastically lowered the short tubes' content, which led the authors to conclude that tip–tip collisions had a prime role in the growth process of Ge-imogolites. Using an analogical approach, Yucelen et al. [70] described the growth kinetics of Si- and Ge-imogolites. The authors shifted from a dissolution–precipitation mechanism to precursor addition growth, which probably had a stronger correlation with the precursor's initial concentration. However, this might be valid only during the initial growth stages, when this concentration is high. The combination of this mechanism with oriented attachment enabled the description of both the length distribution and average length value evolution for the range of initial precursor concentration P_0 (Figure 18).

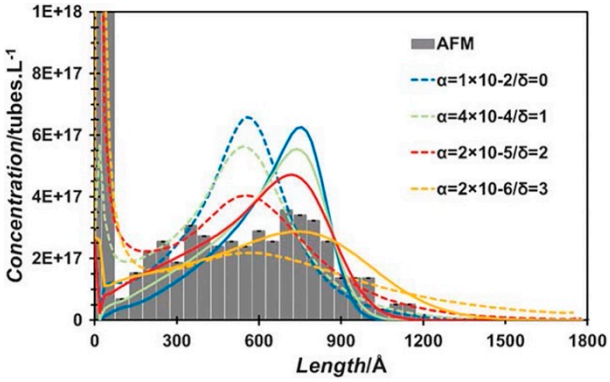

Figure 17. Final single-walled length distribution considering a dissolution mechanism for four different sets of kinetic parameters. Dotted lines are used for calculations using the tip–tip collisions hypothesis and straight lines are used for the dissolution hypothesis. From [69] with permission from the PCCP Owner Societies.

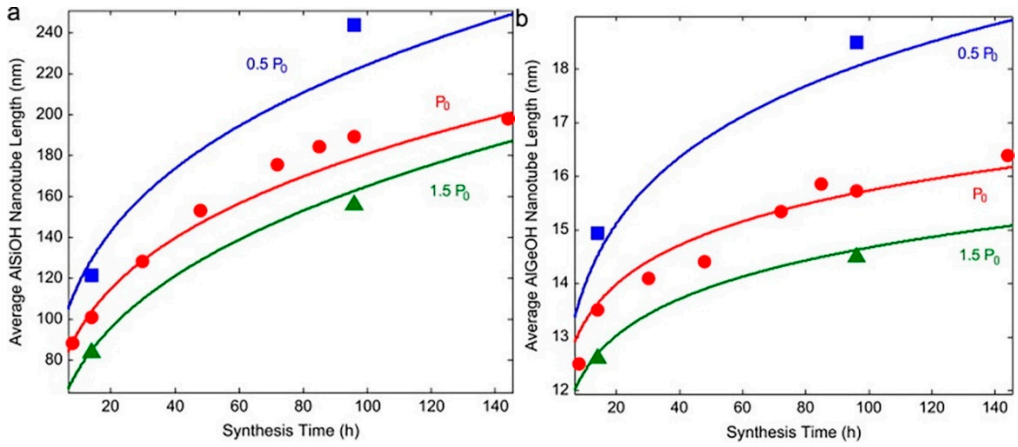

Figure 18. Comparison between the experimental (symbols) and model predictions (curves) of the mean length of (**a**) the aluminosilicate nanotubes, and (**b**) the aluminogermanate nanotubes, as a function of the synthesis time and the initial precursor concentration, from [70]. Copyright ©2012 Elsevier Ltd., Amsterdam, The Netherlands.

2.3. Direct Introduction of Sheet Size Difference into the Energy Equations

Very few theoretical papers have been devoted to the study of the cation substitution effect on the morphological features of hydrosilicate nanoscrolls. This was one of the reasons for the modification of the energy Equations (1) and (2) made in [71]. The modification introduced the radius of the mechanically unstressed layer r_0 into the strain energy component:

$$E_s = \frac{Yh^3}{24(1-\mu^2)}\left(\frac{1}{r} - \frac{1}{r_0}\right)^2 \tag{3}$$

where Y is the Young's modulus, h is the full thickness of the layer, μ is the Poisson ratio and r is the current radius of curvature. The proportionality $1/R^2$ in Equations (1) and (2) originated from the analytical modelling of carbon nanotubes' strain energy. In such a case, the flat carbon layer would indeed be stress-free, but it seems not to be so in the case of the hydrosilicate layer. The introduction of a surface tension difference term does not eliminate the issue completely, because there is a risk of overestimation of the surface tension (specific surface energy) value. The proposed correction effected a kind of role reassignment between strain and surface energy terms and a separation of the two scrolling drivers. For example, there are artificial structures that scroll only due to the lattice misfit between

sheets [72,73]. Conversely, there are layers that grow and scroll—with a micron scale diameter—at the gas/liquid interface, merely due to a large surface energy difference [74].

The r_0 value could be expressed in terms of the sheet size, in the following approximation, assuming an equal thickness of the outer and inner sheets:

$$r_0 \approx \frac{h}{4}\frac{l_a + l_b}{l_a - l_b} = \frac{h}{4}\frac{k+1}{k-1} \tag{4}$$

where l_a and l_b are the specific sizes of the two sheets, $l_a > l_b$. The choice of l_a and l_b depends on the particular case. Their values could be equal to the hydroxide lattice constant, or proportional to the number of polyhedrons. Some of the specific sizes are shown in Figure 4. In the case of imogolite, these sizes are the distance between two oxygens in the gibbsite sheet and the size of the side of the silica tetrahedron.

Figure 19 presents r_0 as a function of the $k = l_a/l_b$ ratio. The correct r_0 value calculation would be the first step for the prediction and design of hydrosilicate nanoscrolls' morphology. The direct implementation of the sizes taken from Figure 4 yielded $r_0 = 0.96$ nm ($k = 1.23$) for imogolite (compared with 0.99 nm [29,32,41,42]), $r_0 = 4.58$ nm ($k = 1.04$) for halloysite (compared with 3.3 nm [56]) and $r_0 = 4.91$ nm ($k = 1.04$) for chrysotile (compared with 8.8 nm [58]). Obviously, the use of hydroxide lattice constants generates an error that become crucial in the estimation of large r_0 values, due to the form of the function. For example, if the lattice constant $a = 0.3085$ nm for partially dehydroxylated $Mg(OH)_2$ (dehydroxylation would indeed be needed to attach the silica network) were to be used [75], the value would be $r_0 = 9.76$ nm ($k = 1.02$), which is much closer to the DFT-obtained value.

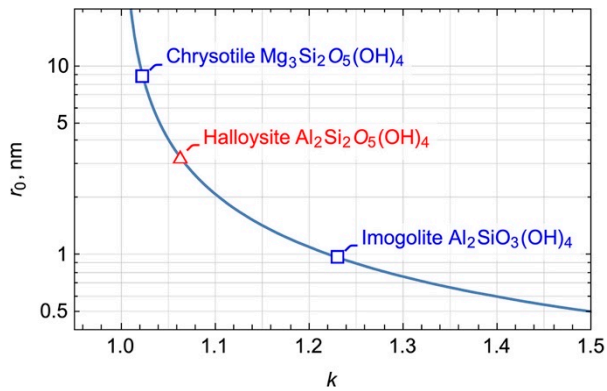

Figure 19. Dependence of the radius of the mechanically unstressed layer on the relative sheet size difference ($h = 0.4$ nm). The square symbol indicates that the octahedral sheet is the outer one. The triangle symbol indicates that the tetrahedral sheet is the outer one.

Another way to overcome this issue is to use DFT-obtained values, which are more precise as reference points for continuous modelling. Then, the r_0^* value of a new nanotubular compound obtained by cation substitution could be expressed through the r_0 of a starting reference compound, assuming the constant size of one of the sheets. For example, in the case of $Ni_3Si_2O_5(OH)_4$ the r_0^* value would be [76]:

$$r_0^* = \frac{h}{4}\frac{b^*\left(r_0^{chr} + h/4\right) + b^{Mg}\left(r_0^{chr} - h/4\right)}{b^*\left(r_0^{chr} + h/4\right) - b^{Mg}\left(r_0^{chr} - h/4\right)} \tag{5}$$

where $r_0^{chr} = 8.8$ nm and b^* and b^{Mg} are specific sizes of $Ni(OH)_2$ and $Mg(OH)_2$, respectively. The equation yielded a figure of 15 nm in this case. If the direction of scrolling is opposite with respect to the reference structure [77]:

$$r_0^* = \frac{h}{4}\frac{b^{Mg}\left(r_0^{chr} - h/4\right) + b^*\left(r_0^{chr} + h/4\right)}{b^{Mg}\left(r_0^{chr} + h/4\right) + b^*\left(r_0^{chr} - h/4\right)} \quad (6)$$

This equation yielded $r_0^* = 3.25$ nm for halloysite (chrysotile as reference), which is in good agreement with the previously published results [56]. The same equations could be obtained in the case of tetrahedral substitution, assuming the constant size of the octahedral sheet. An intermediate compound could be calculated using Vegard's law approximation.

To conclude, the estimation of the r_0 value on the basis of the crystal structure is rather simple but great care must be exercised. The Equations (4)–(6) should be used as a valid initial approximation, followed by DFT refinement, if possible.

By using Equation (3) together with the surface energy equation (which was almost equal to the second term of Equation (2)), Krasilin and Gusarov [71] revealed two general cases of scrolling (Figure 20). The action of strain attempted to bend the layer in such a way that the larger sheet became the outer one. In addition, it stabilised the radius of curvature around r_0 in order to minimise strain. On the other hand, the forces caused by surface energy difference attempted to bend the layer in such a way that the sheet with the higher σ became the inner one in order to minimise its surface area. With respect to the flat layer, the surface energy difference could amplify bending and scrolling (curves 4 and 5 in Figure 20a) or compete with the action of strain (curves 1 and 2). It is noteworthy that, according to a number of papers devoted to $Mg(OH)_2$, $Al(OH)_3$ and SiO_2 specific surface energy calculations [78–81], hydroxides have $\sigma \approx 0.1 - 0.2$ J/m^2 whereas corresponding oxides have $\sigma \approx 1.5$ J/m^2. Therefore, all of the layers that would prefer halloysite-type scrolling would experience some difficulties because of strain/surface energy competition [77].

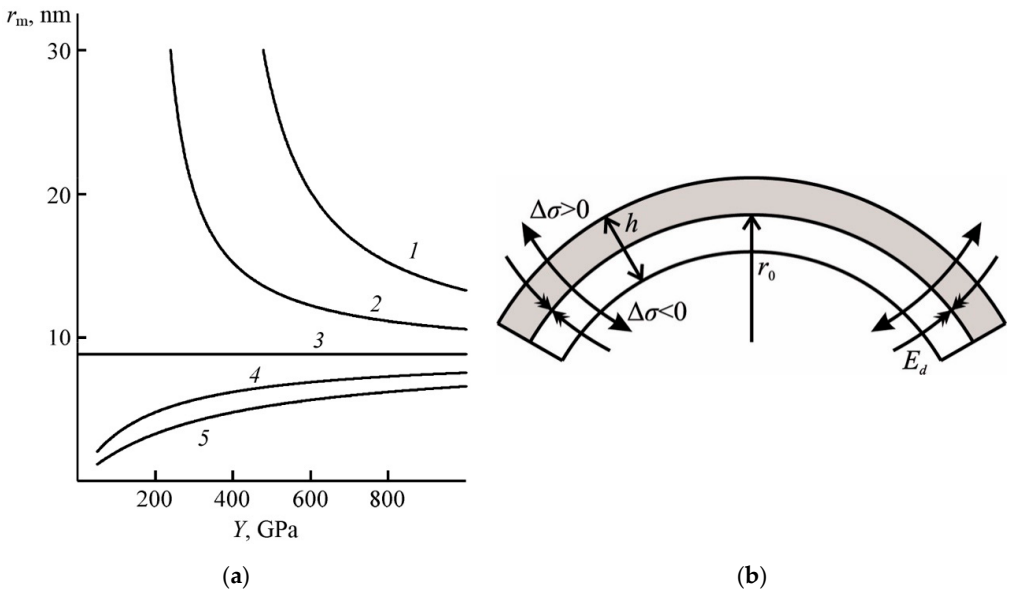

Figure 20. (**a**) Dependence of the nanotube radius at the total energy minimum on the Young's modulus at $\Delta\sigma$ (1) 0.6, (2) 0.3, (3) 0, (4) −0.3 and (5) −0.6 J/m^2. (**b**) Bilayer bending model. Both images are from [71]. Copyright ©2014 Pleiades Publishing, Ltd., New York, United States.

Krasilin and Gusarov [82] expanded the single-walled case to multi-walled chrysotile scrolling, assuming an Archimedean spiral form of the cross-section, a cylindrical form of the nanoscroll and the free slipping of adjacent layers. The former assumption made it possible to consider the scroll to

be of an unlimited (in terms calculation) number of layers, as mentioned in [65], in order to find its energy minimum (Figure 21). A kink in the curve, shown in Figure 21, corresponded to the beginning of multi-walled scrolling with a large energy effect due to adhesion.

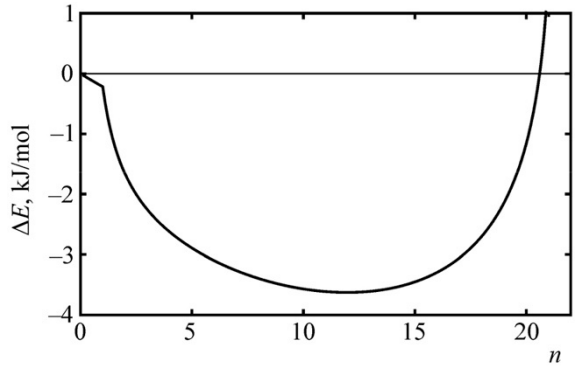

Figure 21. Change in the energy effect of scrolling as a function of the number of layers of the nanoscroll, from [82]. Copyright ©2015 Pleiades Publishing, Ltd., New York, United States.

Finally, by increasing the cell size (the length of the Archimedean spiral or the length of the cylinder), the energy model could simulate the equilibrium nanoscroll growth process. The study [83] demonstrated a correlation between the outer and inner diameters of 'growing' nanoscrolls that depended on the structural parameters of the model (Figure 22). A simultaneous increase in the outer and inner diameters was caused by the same conflict between the strain and surface energy (Figure 20). An important result was the observation of a general energy minimum of 'growing' single- or multi-walled nanoscrolls, which can now be compared with the sizes of multi-walled nanoscrolls obtained in the experiment.

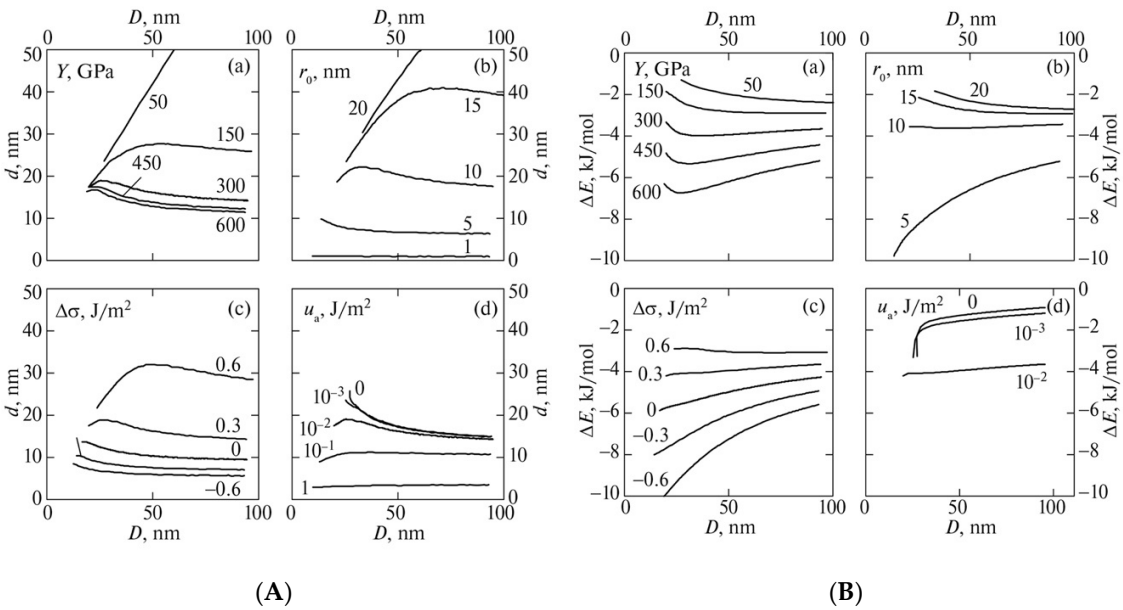

Figure 22. (**A**) Influence of Young's modulus, curvature radius, specific surface energy difference and the specific adhesion energy on the relationship between the optimum internal and external diameters of a scroll during its radial growth. (**B**) The energy effect of the radial growth of nanoscrolls with various values of Young's modulus, curvature radius, specific surface energy difference and specific adhesion energy. Both images are from [83]. Copyright ©2016 Pleiades Publishing, Ltd., New York, United States.

Summarising this part of the review, we would like to underline the need of the adequate parametrisation of the energy model. For example, the model [83], discussed above, includes three energy components: strain, surface, and adhesion energy.

Young's modulus and the r_0 are key parameters for the estimation of the strain energy. The latter can be determined by either using specific sizes l_a and l_b through the Equation (4), or by using the reference structure and the Equations (5)–(6). Metal oxides, metal hydroxides lattice constants, and the sizes of single metal–oxygen polyhedrons can be used as the specific sizes. Young's modulus has to be chosen on the basis of experiment or theoretical calculations. The DFT calculations [42,56,57] predicted Y in the range of 200–400 GPa for the hydrosilicate nanotubes. This range can be a reasonable approximation for the energy model.

Specific surface energies of all surfaces have to be determined for the surface energy calculation. It is reasonable to assume that, due to hydroxylation, the specific surface energies of metal hydroxide and silica sheets would be around 0.1 J/m^2 [79,80] and 1.5 J/m^2 [78], respectively. These values can be obtained firstly by the DFT calculations. Second, assuming the crystal structure is known, the specific surface energy can be calculated as an energy of broken bonds along some plane (*hkl*), as it was carried out in [78]. Third, the specific surface energy can be determined in a calorimetric experiment. It can be assumed that the specific surface energies of the edge surfaces are at least two times higher than the specific surface energies of outer or inner surfaces. However, the precise estimation of these values is still questionable. Another issue, that should be discussed here, is related to the size (curvature) dependence of the specific surface energy. A decrease in the particle size below 3–5 nm causes a decrease in the specific surface energy down to 0 [84,85]. In the case of multi-walled chrysotile and halloysite nanotubes, this feature can be negligible, but it might have an effect on imogolite morphology. In other words, the imogolite layer can, probably, scroll primarily due to the strain, because specific surface energy difference on the opposite sides of the layer will be eliminated by the high curvature.

In analogy with the surface energy, the specific adhesion energy can be determined as a number of hydrogen bonds per surface area. The energy of a single hydrogen bond can be estimated as a function of interlayer spacing by an empirical equation, proposed, for example, in [86]. Assuming a 0.3 nm interlayer spacing in hydrosilicates, the specific adhesion energy is around 0.1 J/m^2. Some particular parametrization cases can be found elsewhere [65,76,77].

3. Morphological Features Related to Cation Doping

Figure 23 shows r_0 values for a number of 3:2 chrysotile-, 2:1 imogolite- and 2:2 halloysite-like (*Me*:Si ratio) structural derivatives, calculated using Equations (4)–(6). It is important to note that the left branch ($k < 1$) is shown for the illustrative purpose to underline the opposite direction of scrolling of certain structural derivatives. Formally, all the symbols belong to the right branch (see Figure 19). The synthesis of some of these compounds will be discussed below, in the light of the r_0 value change. The specific sizes l_i were adopted from the following papers: $Ni(OH)_2$ [87], $Co(OH)_2$ [88], $Fe(OH)_2$ [89], GeO_2 [90], TiO_2 [91] and CoOOH [92].

Other useful information can be obtained with the help of the energy theory of isomorphous substitutions. The following equation for an enthalpy of mixing was proposed by Urusov [93]:

$$\Delta H_{\mathrm{mix}} = x(1-x)cq\left[x\zeta_g + (1-x)\zeta_h\right]\left(\frac{\Delta R}{R_{\max}}\right)^2 \tag{7}$$

where x is the mole fraction, $c = 104.6$ kJ/mol is a material-dependent parameter, q is the coordination number of the substituted position and ζ_g and ζ_h indicate the number of atoms and their valency in the two compounds based on guest and host atoms as $\zeta = mz_{\mathrm{M}}z_{\mathrm{A}}$, where m is the number of atoms and z_{M} and z_{A} are the valency of the cation and anion. In the case of a complex oxide, the ζ value can be obtained by decomposition: $\zeta\left(Mg_3Si_2O_5(OH)_4\right) = 3\zeta(MgO) + 2\zeta(SiO_2) + 2\zeta(H_2O) = 3(2{\cdot}2{\cdot}2) + 2(3{\cdot}4{\cdot}2) + 2(3{\cdot}1{\cdot}2) = 84$. ΔR is the difference between the cation–anion (metal–oxygen) distances (that are calculated on the basis of effective ionic radii) of the guest and the host cation, and

R_{max} is the maximal distance. These values were calculated on the basis of the effective ionic radii system proposed by Shannon and Prewitt [94]. Figure 24 shows the calculation results, which will be compared with the phase composition of hydrothermal treatment products. Generally, the high enthalpy of mixing speaks in favour of immiscibility and by-product formation.

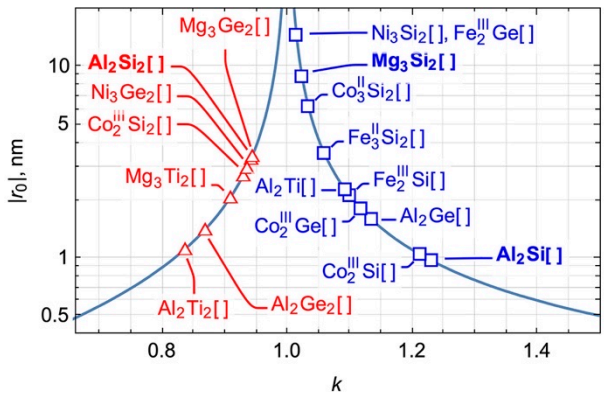

Figure 23. Two branches of $r_0(k)$ and the estimated r_0 values for a number of hydrosilicate derivates (h = 0.4 nm). Square brackets reduce the standard anionic part, for example: $Mg_3Si_2[O_5(OH)_4]$, $Al_2Si_2[O_5(OH)_4]$, $Al_2Si[O_3(OH_4]$, etc. The square symbol means that the octahedral sheet is the outer one and the triangle symbol means that the tetrahedral sheet is the outer one.

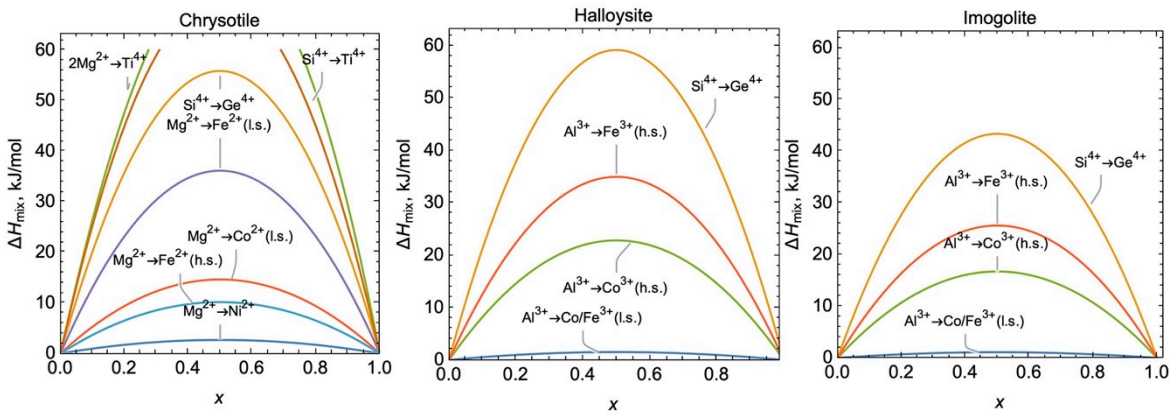

Figure 24. The calculated enthalpies of mixing in chrysotile, halloysite and imogolite vs. the mole fraction of a guest cation x. 'l.s.' means low spin configuration, 'h.s.' means high spin configuration.

3.1. Change in Size Parameters, Platy Morphology and Formation of By-Products

Changes in the nanotube diameter and length, the formation of plates instead of tubes and the formation of by-products (usually metal oxides) are among the most common effects of cation doping. First, it is interesting to compare Si^{4+} to Ge^{4+} substitutions, because these were made for all three of the hydrosilicates. In the case of imogolite, the substitution led to the formation of double-walled nanotubes with an increased outer diameter [65,95]. The estimated r_0 value for $Al_2GeO_3(OH)_4$ was 1.6 nm (Figure 23), in comparison with 0.96 nm for $Al_2SiO_3(OH)_4$, which favoured the formation of poly-walled structures. The substitution of Si^{4+} by Ge^{4+} in $(Mg/Ni)_3Si_2O_5(OH)_4$ resulted in the formation of platy particles [5,64,96]. In fact, the size difference between the two sheets, here, became even stronger, but the direction of potential scrolling changed to the halloysite-type (Figure 23). We believe that $(Mg/Ni)_3Ge_2O_5(OH)_4$ encounters the same hindrance as synthetic halloysite scrolling, which is, generally, the conflict between strain and surface energy [77]. In the case of $Al_2Si_2O_5(OH)_4$ halloysite (Figure 25), Ge^{4+} favoured scrolling [97] and decreased the r_0 value of the layer down to 1.4 nm. Unfortunately, little attention has been paid to the phase composition of systems with partial Si^{4+} to Ge^{4+} substitutions, and this could be important in the context of high ΔH_{mix} values (Figure 24).

White et al. [97] claimed that they obtained Ge-doped imogolites with a high Ge content (Figure 25d); the work [65] assumed unlimited miscibility, and X-ray diffraction was not involved [64]. The probable increase in Si–Ge miscibility in imogolite could be related to a decrease in dimension, from a 2D SiO_2 network in halloysite and chrysotile to 1D or even 0D [98,99].

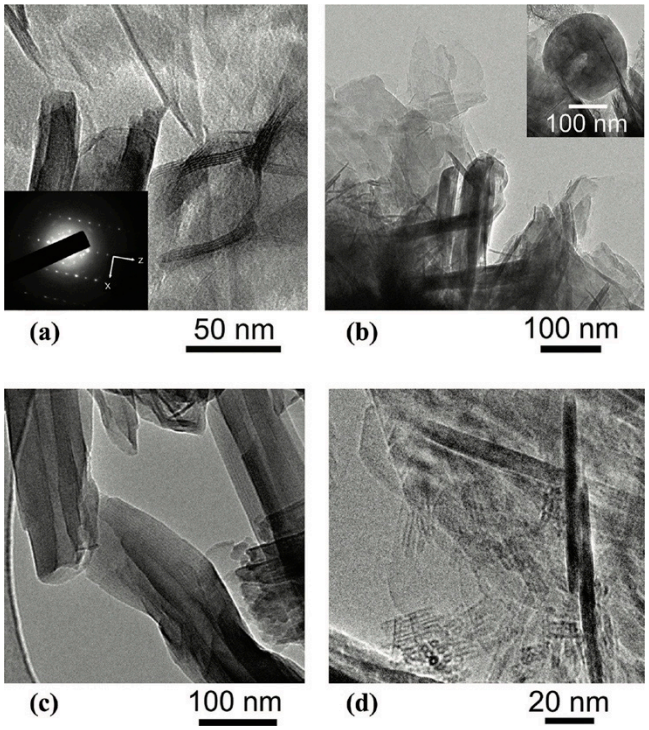

Figure 25. Electron microscope and electron diffraction images of the nanostructures obtained after 7 days of hydrothermal reaction between $Al(OH)_3$ and SiO_2 in the presence of GeO_2, at pH 2 and a temperature of 220 °C. The molar fraction of added GeO_2 was (**a**) 0, (**b**) 0.05, (**c**) 0.1 and (**d**) 0.5. The inset in (**b**) shows a spheroidal kaolinite particle, from [97]. Copyright ©2012 American Chemical Society, Washington, United States.

The next case is cation substitution by Ti^{4+}. Although this cation prefers octahedral sites, the difference between Mg^{2+} and Ti^{4+} charges would not allow large miscibility. Moreover, the effective ionic radii of Ti^{4+} in VI and IV coordination did not fit with those of Mg^{2+} and Si^{4+}, making the ΔH_{mix} value the highest among the other cases shown in Figure 24. Nevertheless, several attempts at Ti-doped chrysotile synthesis were carried out. Bloise et al. [100] synthesised Ti-doped chrysotile by the hydrothermal alteration of Ti-doped forsterite with a TiO_2 content in the 0.3–1 wt.% range (X-ray spectroscopy analysis). The authors estimated the mean outer diameter of 200 nanotubes to be 70 nm. The highly crystalline forsterite required an increased hydrothermal treatment time up to 384 h. The role of pressure was also studied: an increase in the pressure shortened the nanotubes' length from a maximum of 30 μm at 1 kbar to 3 μm at 2 kbar. At the end of the treatment, the system contained several phases together with nanotubes. Maslennikova and Gatina [101] performed the synthesis (Figure 26) using $Ni(OH)_2$, $NiSiO_3$ and TiF_4 as starting components. At the minimum TiF_4 content of 10 wt.%, the system already contained montmorillonite and nickel titanate as by-products.

Doping by $Fe^{2+/3+}$ could occur in both the octahedral and tetrahedral sites of the structure. The calculated ΔH_{mix} value strongly depended on the type of cation configuration (low spin or high spin). With Fe^{2+}, the main problem was that the oxidation process was intensified by high pressure hydrothermal conditions. Korytkova et al. [102] studied $(Mg,Fe)_3Si_2O_5(OH)_4$ formation, choosing $(Mg,Fe)SiO_3$ and (Mg,Fe)O as starting components. The authors mentioned an increase in Fe^{3+} content with an increase in the total Fe content in the system. It was nevertheless possible to obtain single-phase

$(Mg,Fe)_3Si_2O_5(OH)_4$ tubes or plates if the initial FeO content was below 15–20 wt.%. The average outer diameter of the tubes increased from 30 to 60 nm with an increase in Fe content, whereas the r_0 for $(Mg,Fe^{2+})_3Si_2O_5(OH)_4$ was lower than that for pure chrysotile (Figure 23). This means that a sufficient amount of Fe^{2+} was oxidised, (or another effect, discussed in Section 3.2, below, took place): this affected at least half of the total iron content, according to the author's estimation. Another attempt at Fe^{2+} stabilisation was reported in [103]. The authors used several types of starting mixture containing FeO and $FeCl_2{\cdot}4H_2O$, sealed in Pt ampules by an arc welding technique. Most probably, the presence of a shielding gas inhibited (but did not exclude) the subsequent oxidation of iron during hydrothermal treatment. The authors reported on $Fe_3Si_2O_5(OH)_4$ nanotube formation with diameters in the 8–70 nm range. Others [104,105] have considered the effect of Fe^{3+} doping on chrysotile structure and morphology. The authors estimated the molar content of Fe^{3+}, normalised to the sum of Mg and 1.5Fe (including one vacancy per two iron cations), at which the stabilisation of plates occurred, to be 7 at.%. A further increase in Fe^{3+} up to 22 at.% led to the formation of Fe_2O_3. Mössbauer spectroscopy determined the maximum Fe^{3+} content in hydrosilicate at 12 at.%. Unfortunately, the spectra did not allow a distinction to be made between the octahedral and the possible tetrahedral positions of iron. The authors assumed that the increased width of the Mössbauer peaks originated from Fe^{3+} distributed along a number of slightly different positions, due to at least four possible substitution schemes, and possible distortion because of the curvature effect. The spectroscopic experiments of Borghi et al. [106] and Shafia et al. [107] demonstrated that Fe^{3+} preferred a high spin configuration in both Fe-doped chrysotile and imogolite. This can explain the Fe_2O_3 formation along with Fe-doped imogolite after reaching around 3 at.% of iron content [107], because otherwise (in the case of a low-spin configuration) the components should have been easily miscible (Figure 24). In another research study [108], the average diameter of 450 Fe-doped imogolite nanotubes was estimated as 4.4 nm, and this value was at least two times larger than that of pure imogolite. This fact is in good agreement with the r_0 value calculation (Figure 23) in the case of imogolite doping by Fe^{3+}.

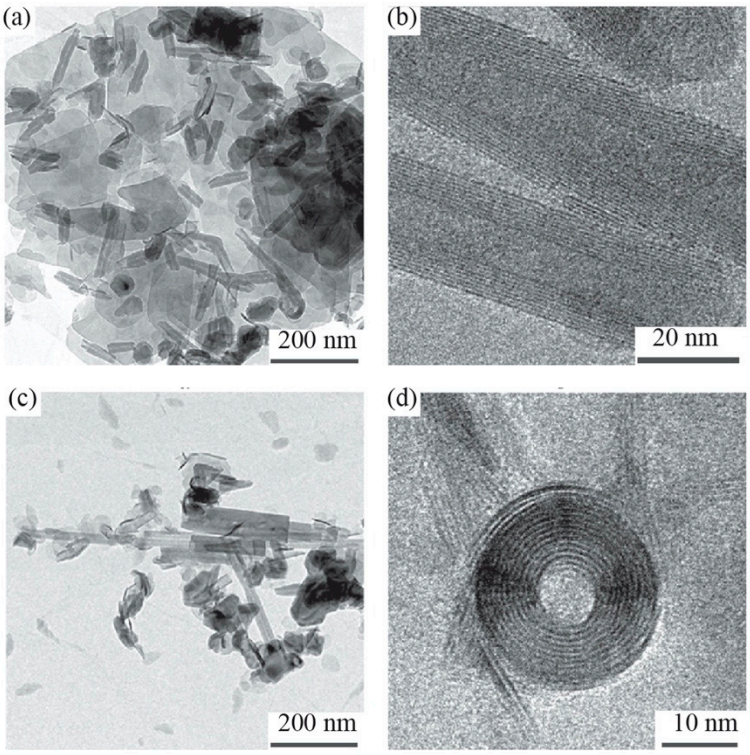

Figure 26. (**a**–**d**) Transmission electron microscopy of the Ti-doped chrysotile nanotubes, from [101]. Copyright ©2018 Pleiades Publishing Ltd., New York, United States.

Only a few papers have been devoted to $Co^{2+/3+}$ substitutions in chrysotile [109,110]. Korytkova et al. [109] reported a continuous decrease in the outer (from 25 to 10 nm) and inner diameters (from 5 to 2 nm) with an increase in Co content in the system, and this was in accordance with the r_0 value change (Figure 23). Most synthesis products contained additional phases, such as cobalt silicate, oxides and platy particles. The latter were formed, probably, due to partial cobalt oxidation in hydrothermal conditions, which is analogous to the case of iron. It is interesting to note an idea related to $Fe^{2+/3+}$ and $Co^{2+/3+}$ transition. The oxidation process leads to a stepwise change in the effective ionic radii of these cations and in turn, to a change in the size difference between the sheets. Could the morphology of Co^{2+}- or Fe^{2+}-doped nanoscrolls be further tuned—transformed into a plate or scrolled even more, depending on the case—by oxidation?

Nickel is a frequently used dopant in chrysotile synthesis. The ionic radius, which is close to Mg^{2+}, and low ΔH_{mix} make two cations miscible in any ratio. The reported data on its nanotube diameter are fairly controversial. Korytkova et al. [111] observed a decrease in the outer diameter from 30 to 15 nm, and a decrease in the inner diameter from 5 to 3 nm as the Ni content in the system increased. McDonald et al. [112] obtained $Ni_3Si_2O_5(OH)_4$ nanotubes with an outer diameter of 25–30 nm and an inner diameter of about 10 nm (Figure 27). White et al. [113] reported on the following $Ni_3Si_2O_5(OH)_4$ sizes: 20–35 nm outer diameter and 7–25 nm inner diameter.

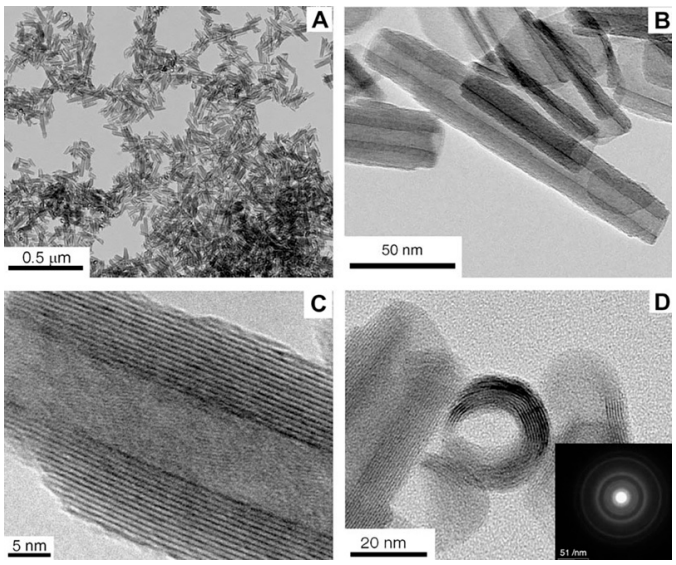

Figure 27. TEM micrographs of nickel 1:1 phyllosilicate: (**A**) the general view, (**B**) the side view of a tubular particle, (**C**) the higher magnification view showing the hollow multiwall tubular structure and (**D**) the end-on view of one of the tubes (Inset: electron diffraction pattern). From [112]. Copyright ©2008 Elsevier Inc., Amsterdam, The Netherlands.

Finally, Krasilin et al. [114] synthesised tubes with mean outer and inner diameters of 40 nm and 10 nm, respectively. The estimation of the r_0 value (Figure 23) predicted a diameter increase during the Mg^{2+} to Ni^{2+} substitution in the chrysotile structure. Most probably, the opposite tendency was caused by the choice of starting components and the hydrothermal synthesis conditions. The influence of the presence of NaOH during the synthesis of $Mg_3Si_2O_5(OH)_4$ and $Ni_3Si_2O_5(OH)_4$ nanotubes was demonstrated in [76]. Figure 28 combines electron microscopy statistics with the energy modelling of finite mass layers scrolling [76]. The preferable number of layers n_p was 12–13 in the case of the Mg- and 25–26 in the case of the Ni-based layer, independent of mass. The size parameters of all the nanoscrolls of a certain mass were situated within an energy equal area close to the energy minimum. In this area, short nanoscrolls with $n > n_p$ and long nanoscrolls $n < n_p$ were equal in terms of the energy effect of scrolling. According to the model, the area grew continuously with an increase in mass. Scatter plots showed the differing response of Mg- and Ni-containing systems to the presence of NaOH.

Apart from the difference in $Mg(OH)_2$ and $Ni(OH)_2$ solubilities, the distance between the 'starting point' of nanoscroll growth (approximately 3–4 layers, 20–50 nm length) and the energy minimum n_p could matter. Synthesis in the water allowed the nanoscrolls of both compositions to grow up to 30 layers thick, and the mean diameter of the $Ni_3Si_2O_5(OH)_4$ nanoscrolls was indeed smaller than that of $Mg_3Si_2O_5(OH)_4$. In the case of $Mg_3Si_2O_5(OH)_4$, growing up to 30 layers was enough to occupy both the energy equal states with $n < n_p$ and $n > n_p$. Conversely, most of the $Ni_3Si_2O_5(OH)_4$ nanoscrolls still had $n < n_p$. The addition of NaOH intensified recrystallisation, but because $Mg_3Si_2O_5(OH)_4$ nanoscrolls had already occupied both types of equal states, only an increase in length was observed. In turn, $Ni_3Si_2O_5(OH)_4$ nanoscrolls demonstrated an increase in both the diameter and length in order to occupy both types of energy states. The resulting average diameter of $Ni_3Si_2O_5(OH)_4$ was larger, in that case.

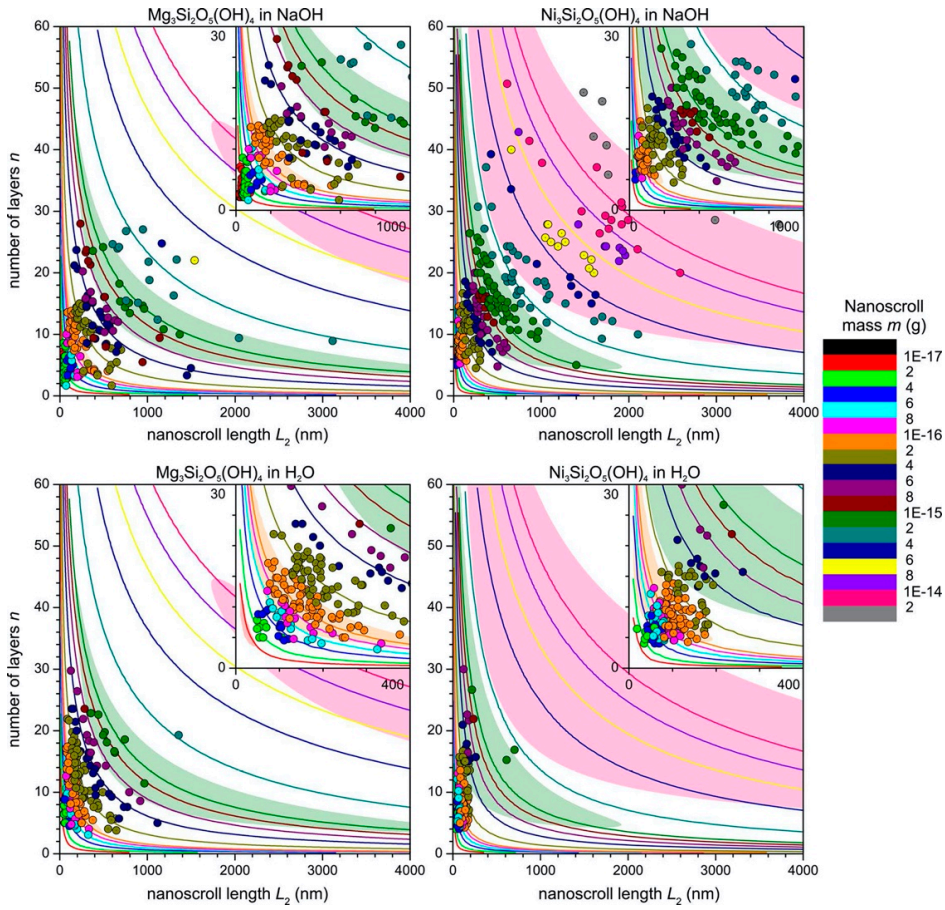

Figure 28. Growth of Mg-chrysotile and Ni-pecoraite. The points are nanoscrolls, measured using an electron microscope, and the solid curves are modelling results. The coloured areas are 500 J/mol regions around the energy minimum modelled for nanoscrolls of different mass, from [76]. Copyright ©2017 American Chemical Society, Washington, United States.

3.2. Tubes-in-Tubes, Cones and Cation Distribution

Often, the simultaneous presence of several isomorphous cations gives rise to several additional morphological features. One of these features is the increased diameter of the mixed composition nanotubes in comparison with single cation-based nanoscrolls. This effect was observed in the case of substitutions by Ge in imogolite [65], and $Fe^{2+/3+}$ and Ni^{2+} in chrysotile [102,115]. In addition, partial substitution resulted in the appearance of nanoscrolls with a complex tube-in-tube (Figure 29) and conical (Figure 30) morphology. Krasilin et al. [116] revealed that partial Mg^{2+} to Ni^{2+} substitution in chrysotile increased conical scroll content from 10% to 40%. We believe that this growth in

morphological diversity was supported by some kind of spatial distribution of isomorphous cations along the layer. In the view of the energy model based on the r_0 value, the strain energy of a multi-walled spiral cross-section could be further minimised, assuming angular dependence $r_0(\varphi)$ [117,118]:

$$E_s = \frac{Yh^3}{24(1-\mu^2)} \int_0^{2\pi n} \left(\frac{1}{r(\varphi)} - \frac{1}{r_0(\varphi)} \right)^2 \sqrt{f^2 + r^2(\varphi)} \mathrm{d}\varphi \tag{8}$$

where f is the Archimedean spiral constant, and $r(\varphi)$ is the current radius of curvature. Thus, the cation, which would cause a larger r_0 value, would concentrate in the outer layers of the scroll, and vice versa. This assumption was confirmed [118,119] by the X-ray spectroscopy of several $(Mg_{0.5}Ni_{0.5})_3Si_2O_5(OH)_4$ nanoscrolls. Figure 31 demonstrates the linear fit of the spectroscopy data with the maximum possible concentration gradient predicted by Equation (8). The spatial distribution along the layer could also cause nonuniform bending momentum and scrolling with an angle, resulting in the formation of cones. Nanotubes and nanoscrolls that have already been formed could serve as seeds for the precipitation of substances enriched with another cation (Figure 29). Korytkova et al. [120] demonstrated that the presence of nanotubular seeds systematically increased the average diameter of $Mg_3Si_2O_5(OH)_4$ nanotubes.

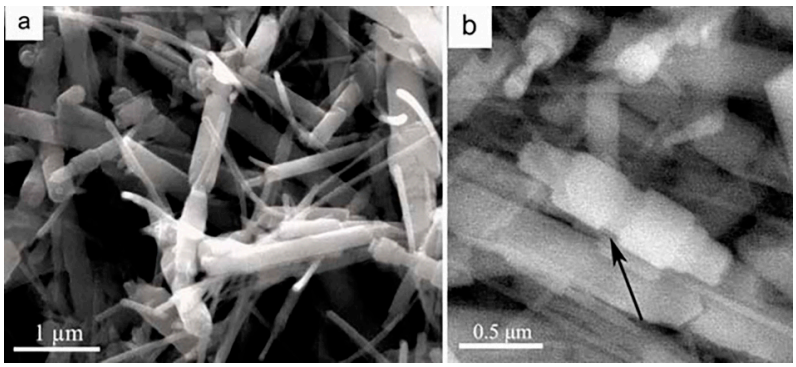

Figure 29. (**a**,**b**) Secondary electron micrographs of Fe-doped chrysotile, from [103]. Copyright ©2009 WILEY-VCH Verlag GmbH & Co. KGaA, Weinheim, Germany.

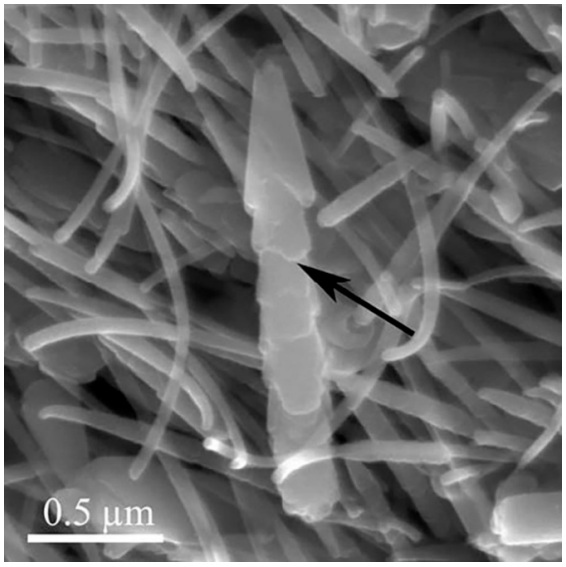

Figure 30. Secondary electron SEM image of the Ti-doped cone-in-cone chrysotile nanotube, from [100]. Copyright ©2009 E. Schweizerbart'sche Verlagsbuchhandlung, Stuttgart, Germany.

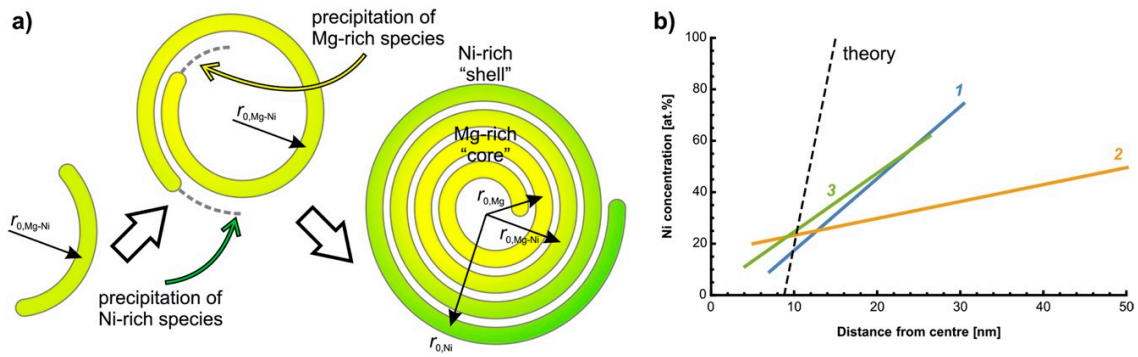

Figure 31. (**a**) Possible mechanism of the Mg^{2+} and Ni^{2+} cation redistribution as a result of the nanoscroll growth process. (**b**) Results of the linear regression of the data obtained by energy-dispersive X-ray spectroscopy in comparison with the maximal gradient (dashed line) predicted by Equation (8), from [118]. Copyright ©2019 Wiley-VCH Verlag GmbH & Co. KGaA, Weinheim, Germany.

3.3. P.S.: Polygonal Serpentine

Polygonal serpentine (PS) is an exotic morphology of a nanotube's cross-section, which was first observed in natural chrysotile samples [25,27,121,122]. However, there was a report which demonstrated the possibility of PS synthesis [123]. Usually, the structure consists of a classic nanotubular core and a polygonal shell of 15–30 sectors (Figure 32). The size of the cross-section can exceed 200 nm. It is interesting to note that the diameter of the nanotubular part is approximately equal to the energy preferable part size predicted in [83]. We believe that polygonisation is one of the stress compensation mechanisms that is activated when the growth in diameter dominates, (for example, in the case of the high oversaturation of a hydrothermal medium). Dódony and Buseck [27] proposed a scheme of sheet rotation in the adjacent PS sectors (Figure 33). According to that scheme, the direction of bending would be opposite in the two adjacent sectors, which would have analogies with antigorite [58]. However, in contrast to wavy antigorite, PS layers remain flat. Another reason for polygonisation could be the spatial distribution of cations discussed in Section 3.2. For example, the doping of chrysotile by a small amount of Al^{3+} (which is very common in nature) resulted in the formation of lizardite plates [124]. The cation can efficiently substitute both Mg^{2+} and Si^{4+} and neutralise the size difference between the sheets. Unfortunately, there is a lack of information regarding the tubular and polygonal parts of PS.

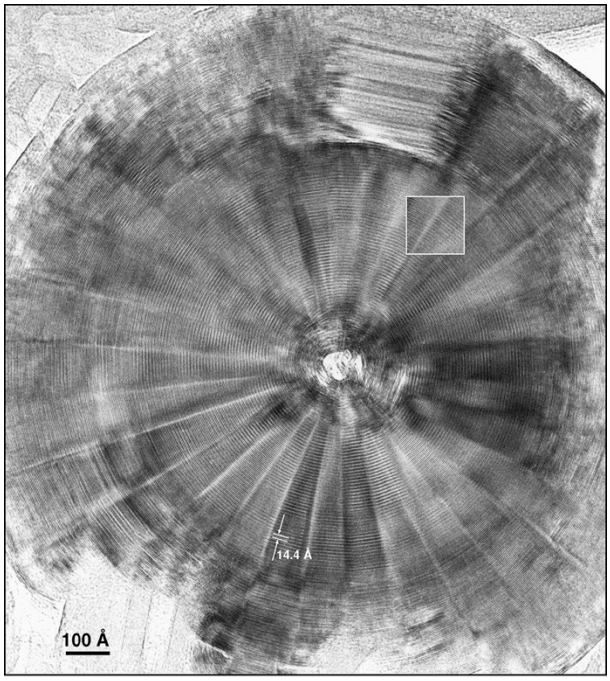

Figure 32. Polygonal serpentine (PS) electron microscope image of a 30-sectored polygonal serpentine viewed down its fibre axis. The inner part of the fibre consists of chrysotile surrounded by a ring of sectors with two-layered lizardite polytypes. The outermost zone of the fibre consists of disordered lizardite. The area in the white box is enlarged in Figure 33, from [27]. Copyright ©2004 by V.H. Winston & Son, Inc., Palm Beach, United States.

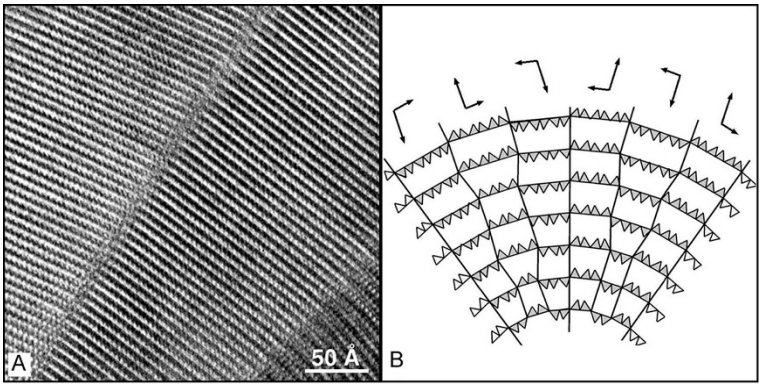

Figure 33. (**A**) Enlarged area indicated in Figure 32, showing offsets of lizardite layers at sector boundaries. (**B**) Schematic sketch of the tetrahedral sheets in a 30-sectored polygonal serpentine. Inversions occur in the sheets at sector boundaries. The polytypes in the adjacent sectors are indicated by their b and c axes, from [27]. Copyright ©2004 by V.H. Winston & Son, Inc., Palm Beach, United States.

4. Properties and Applications Related to Cation Doping

Here, we limited the review to four areas in which cation doping has already been used or could be used in the nearest future. The first area concerns the nanotube porosity design for the adsorption, uptake and release of functional substances. In the second area, nanotubes are used as reinforcing fillers of, generally, different polymers. The third area focuses on the magnetic properties of doped nanotubes. The fourth area is devoted to a number of catalytical applications.

4.1. Tuning Nanotubes' Diameter for Uptake and Release

Sections 2 and 3 demonstrated the theoretical basis for, and the experimental possibility of, tuning hydrosilicate nanotubes' curvature (or even changing the direction of scrolling) by cation doping. This feature could be used for specific surface area (SSA) and pore size control and hence, the control over the amount and speed of uptake and/or release of different substances. From the point of view of the relative impact on morphology and control precision, imogolite seems to be the preferred option: its diameter can be increased almost double by Ge^{4+} doping [65,95,125,126]. Shafia et al. [107] reported on the diameter increase in Fe-doped imogolite, which was in correlation with DFT pore size distribution (Figure 34). Intriguingly, specific surface area also increased, (383 m^2/g for pure imogolite against 455 m^2/g for imogolite doped with 1.4 wt.% Fe), and this might be attributed to the slight change in the contribution of micro- and mesopores observed by the authors. Fe^{3+} doping in chrysotile led to an increase in diameter and a slight decrease in the SSA value from 64 to 54 m^2/g. It is worth noting that the multi-walled nature of chrysotile and halloysite erodes their surface area remarkably in comparison to imogolite. In order to increase those values (up to 200–300 m^2/g), selective acid leaching is often applied [127–129]. It is important to note that variation in synthesis conditions—the type of precursors, the temperature/pressure/time and the hydrothermal medium—can help to tune the diameter and the SSA value of nanotubes [76,113,130,131].

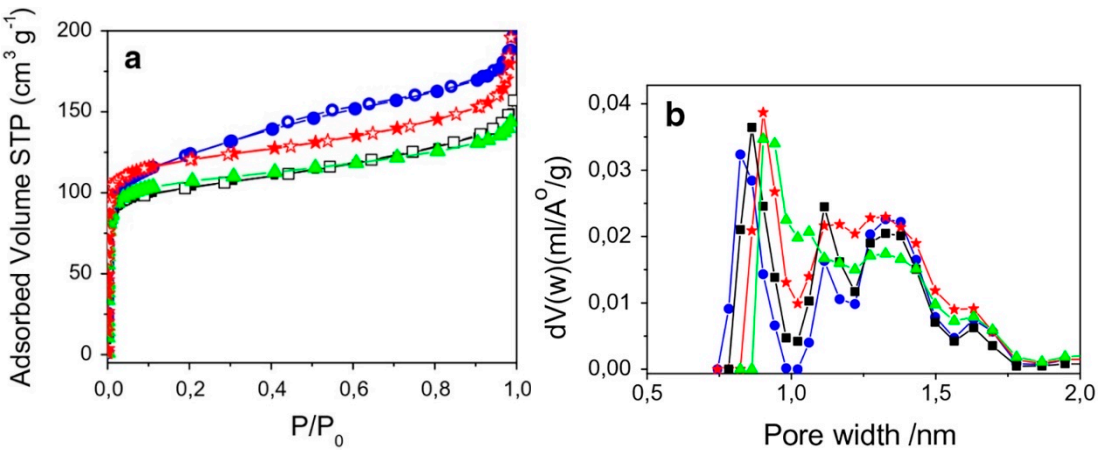

Figure 34. (**a**) N_2 sorption isotherms for the 77 K of pristine imogolite (squares) and imogolite with 0.7 wt.% (stars), and 1.4 wt.% (triangles) Fe^{3+}. Full and hollow symbols refer to the adsorption and desorption branches, respectively. (**b**) Pore size distributions of pristine imogolite (squares) and imogolite with 0.7 wt.% (stars), and 1.4 wt.% (triangles) Fe^{3+}, as obtained by the Non-local Density Functional Theory (NL-DFT) approach method. Both images are from [107]. Copyright ©2015 Springer Science+Business Media Dordrecht, Berlin, Germany.

The nanotubes' porous structure was found to be attractive for the adsorption, uptake and release of a large number of substances, despite systematic studies on the role of the dopant's content not having been carried out. The first group of adsorbed species are gases. Ackerman et al. [132] demonstrated that the uptake of CO_2 and CH_4 decreased by 1.6 times, while 50% of Si was substituted by Ge in imogolite, despite a slight increase in the SSA value. One study [133] achieved 50.6 mg/mL of CH_4 storage capacity at 4.05 MPa by using synthetic imogolite. Gas storage capacity could be further improved by the modification (methylation, for example) of the nanotubes' surface [126,134]. A thorough review [135] considered Mg-containing systems, including chrysotile, as CO_2 capture and recycling materials. In this case, the SSA value remained one of the key parameters.

An additional structural feature of the hydrosilicate nanotubes is their outer and inner surface charge. Depending on the direction of scrolling, halloysite-type nanotubes demonstrate SiO_2-like negative zeta potential value, while chrysotile-type nanotubes have a metal oxide-like positive value [136]. This difference could prioritise the charged species' adsorption from the solution on the

outer or inner nanotube surface. Those species could be surfactants [137–140], metal cations [141–147], anions [148] or dyes [136,149,150]. Thus, the nanotubes could be successfully used as water remediation agents. Applications for compounds that can be loaded into nanotubes vary, from corrosion and the inhibition of unfavourable processes [151–155], to antimicrobial activity [156–158] and medical treatments [159–163].

4.2. Mechanical Properties of Composite Materials

Although the mechanical properties of chrysotile, imogolite and halloysite have been studied theoretically [42,56,57], few experimental data are available. Piperno et al. [53] determined the Young's modulus of pure and Fe^{3+}-doped chrysotile, using an atomic force microscope (AFM), to be 159 ± 125 GPa and 279 ± 260 GPa. Assuming $3Mg^{2+}$ to $2Fe^{3+}$ substitution with the formation of vacancies, an increase in the Young's modulus might appear to contradict some MD calculations [51] discussed in Section 2.2.1. The mean values appeared to depend upon the presence of Fe^{3+}, although the measurements generated a large error. This type of experiment remains very challenging, because of a number of methodological and physical hindrances. One of these is the diameter dependence of the Young's modulus (Figure 35), which has been frequently observed for a wide range of tubular ($Mg_3Si_2O_5(OH)_4$ and $Ni_3Si_2O_5(OH)_4$) and rod-like materials (ZnO, carbon nanotubes) [164–166]. Lecouvet et al. [54] measured the Young's modulus of halloysite nanotubes situated in a pore of a track filter membrane by bending. The authors attributed the increase in small halloysite nanotubes' elastic modulus to the increase in the contribution of surface tension, and a decrease in the elastic modulus in the case of large tubes—to the shear of adjacent layers. In addition, the deformation of large tubes would require a considerable applied force, which could disrupt the nanotube's position by its displacement.

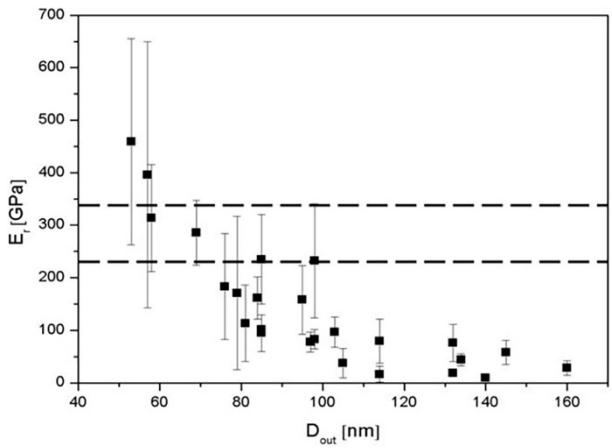

Figure 35. Reduced elastic modulus of the halloysite nanotubes deduced from the force curve measurements as a function of the outer diameter, (error bars indicate one standard deviation). As a comparison, the range of values predicted for the elastic modulus of single-walled halloysite is bounded by the dashed lines, from [54]. Copyright ©2013 IOP Publishing Ltd., Bristol, United Kingdom.

A second set of uncertainties originates from the Young's modulus equation:

$$Y = P\frac{k}{3}\frac{L^3}{D^4 - d^4} \tag{9}$$

where P takes into account boundary conditions, k is bending stiffness, L is the nanotube's length that experiences bending and D and d are the outer and inner diameter, respectively. Regardless of any error in the k value measurement (which could be around 20%), P varies from 1 to 4, depending on whether the ends are clamped or free, and, in practice, it can take on an intermediate value. The L value can be substantially different from the geometric length of a nanotube over a pore and might have to

be determined on the basis of a bending stiffness profile. The error in the outer diameter measurement becomes crucial in the case of small nanotubes, whereas the inner diameter cannot be measured directly using the AFM method. Thirdly, the type of nanotube/AFM tip contact can also affect the results [167]. To conclude, cation doping can be used for tuning the Young's modulus, although great effort must be devoted to obtaining consistent data.

Despite the issues with determining experimental mechanical properties, hydrosilicate nanotubes have been intensively used as reinforcing fillers for polymer composites. A review [168] has highlighted the enhancement of a number of composite functional properties, including mechanics, in comparison to a pristine polymer. In particular, poly(methyl methacrylate) (PMMA) containing 1 wt.% of imogolite nanotubes has demonstrated a 37% increase in the Young's modulus and a 39% increase in tensile strength. Halloysite nanotubes, when injected into different polymers, can also substantially improve mechanical properties [169]. The greatest impact, probably, can be made by ethylene propylene diene monomer (EPDM), a rubber/halloysite composite that can create a tensile strength increase of 874%. Jiang et al. [170] reported a 20% increase in the Young's modulus and tensile strength of the PMMA copolymer/0.5–1 wt.% halloysite nanotubes composite. Synthetic chrysotile nanotubes and natural halloysite were used as fillers for chitosan fibres [171]. The authors demonstrated that the tensile strength increase in the chrysotile-containing composite was remarkably higher (67%) than that of the halloysite-containing composite (5%). Wu et al. [172] reported a 25% Young's modulus increase in the case of a polyimide filling with 4 vol.% of synthetic chrysotile.

Of course, the evidence of polymer reinforcement with nanotubes is not limited to the papers reviewed above, but a thorough investigation would be beyond the scope of the current paper. Despite cation doping's influence on nanoscrolls' mechanical properties, a systematic study of its role in the preparation of composite materials is yet to be carried out.

4.3. Magnetic Properties

Being composed of p-elements, chrysotile, imogolite and halloysite are diamagnetic materials. However, the substitution of Mg^{2+}, Al^{3+} and Si^{4+} cations by elements with uncoupled electrons could enhance the magnetic properties of those nanotubes. The case of $Ni_3Si_2O_5(OH)_4$ nanotubes' magnetic response was studied in [114]. The particles demonstrated a ferromagnetic order (Figure 36) with the Curie point at 23.7 K. Magnetic ordering occurred through a large interlayer distance of 0.73 nm between the adjacent octahedral sheets. The type of ordering qualitatively correlated with that of α-$Ni(OH)_2$ in terms of there being a relatively large interlayer distance. According to [173], the type of magnetism depended on the crystal modification (α or β) of the hydroxide. β-$Ni(OH)_2$ had a smaller interlayer distance (4.6 Å) than α-$Ni(OH)_2$ (8.7 Å) and demonstrated an antiferromagnetic order instead. The α-$Ni(OH)_2$ Curie point of 16 K was lower than that of $Ni_3Si_2O_5(OH)_4$ nanotubes, which might, again, be associated with the larger interlayer period of the latter, as if the proximity of Ni-containing octahedral sheets interfered with their magnetic ordering.

Borghi et al. [106] reported on the complex nature of magnetism in the case of Mg^{2+} and Si^{4+} substitution by Fe^{3+}, related to the probable presence of antiferromagnetic and ferromagnetic coupling (Figure 37). In contrast to Ni^{2+} substitution, Fe^{3+} can occupy both octahedral and tetrahedral sites in an uncontrollable ratio, complicating magnetic response. Meanwhile, some analogy has been found in the comparison of the magnetic properties of $Fe(OH)_2$ and $Ni(OH)_2$. Miyamoto [174] demonstrated antiferromagnetic ordering in $Fe(OH)_2$ with a lattice constant (distance between adjacent layers) of 4.605 Å, which is close to β-$Ni(OH)_2$. Perhaps, Fe^{3+} situated in tetrahedral sites acted like a close-lying hydroxide layer inducing antiferromagnetic coupling in Fe-doped $Mg_3Si_2O_5(OH)_4$. If Fe^{3+} were to occupy only the octahedral sites of the structure, there would be a ferromagnetic-type coupling only.

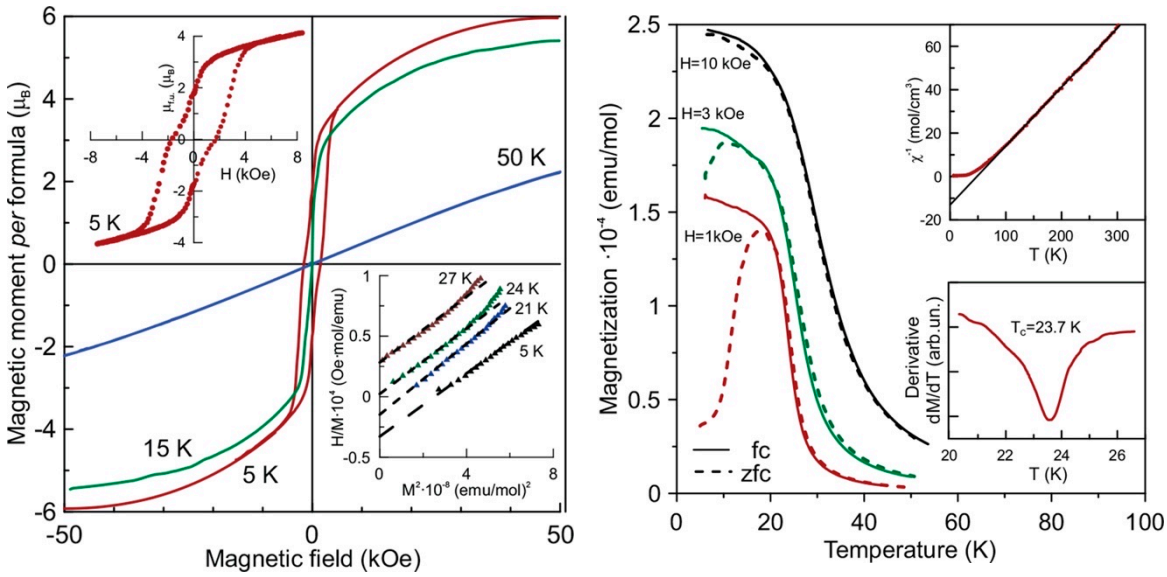

(**a**) (**b**)

Figure 36. (**a**) Magnetisations vs. the applied magnetic field, measured at various temperatures. Upper inset: zoomed low-field part of the hysteresis loop measured at 5 K. Bottom inset: Arrott plots. (**b**) Field-cooled (solid line) and zero field-cooled (dashed line) dc magnetisations vs. the temperature measured in various magnetic fields. Upper inset: reciprocal susceptibility vs. temperature. Red symbols: experimental data; black dashed line: Curie–Weiss fitting. Bottom inset: derivative $\partial M/\partial T$ vs. temperature. Both images are from [114]. Copyright ©2016 IOP Publishing Ltd., Bristol, United Kingdom.

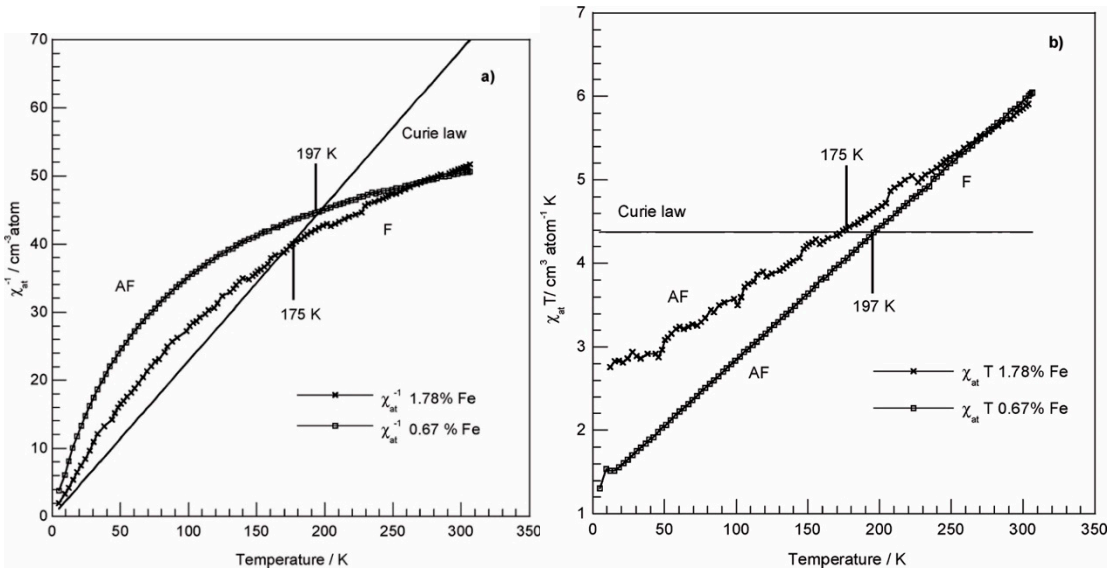

Figure 37. (**a**) Representation of the magnetic behaviour of iron-doped synthetic chrysotile in comparison with the Curie law for the Fe^{3+} high spin ion ($S = 5/2$, Curie Constant $\chi_M T = 4.377$ emu mol^{-1} K): (**a**) χ_{at}^{-1} vs. T experimental data and the representation of the Curie law as $\chi_M^{-1} = f(T)$. (**b**) $\chi_{at}T$ vs. T experimental data and the representation of the Curie law as $\chi_M T = f(T)$. AF–antiferromagnetic coupling; F–ferromagnetic coupling. From [106] with permission from the PCCP Owner Societies.

Another interesting example of obtaining a magnetic response is structure modification through the reduction of dopants by hydrogen or another chemical agent. Ni nanoparticles were obtained by the $NaBH_4$ reduction of $Ni_3Si_2O_5(OH)_4$ nanotubes [175] for application in Li-ion batteries. Obviously, the

appearance of nickel metal makes the composite sensitive to a magnetic field even at room temperature (Figure 38). The dopant reduction reveals the additional applications of nanotubes, for example, as magnetically guided adsorbents, or catalysts.

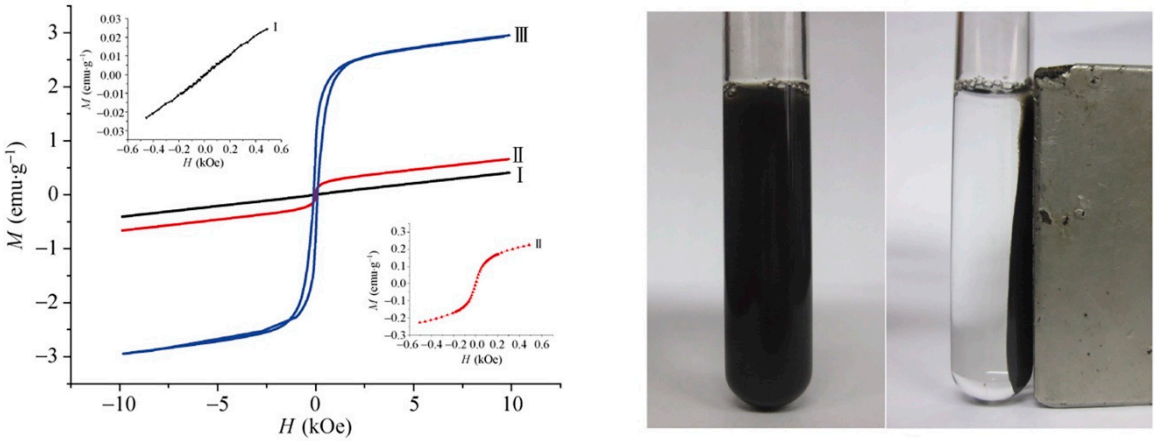

(**a**) (**b**)

Figure 38. (**a**) Magnetisation curves of the $Ni_3Si_2O_5(OH)_4$ nanotubes after the hydrothermal reduction treatment: (I) 120 °C, 10 h; (II) 150 °C, 5 h; (III) 180 °C, 10 h; the inset images in (I) and (II) show partial enlargements. (**b**) Images of the sample of the $Ni_3Si_2O_5(OH)_4$ nanotubes after reduction at 180 °C for 10 h in water, before and after the attraction by a permanent magnet. Both images are from [175]. Copyright ©2011 Tsinghua University Press and Springer-Verlag Berlin Heidelberg, Berlin, Germany.

4.4. Metal Reduction and Catalysis

Among the three hydrosilicates, the hydrogen reduction of doped chrysotile and the related phyllosilicates for catalytical applications constitute the most developed field. Early studies determined the starting temperatures for *d*-elements reduction in chrysotile—they were 400 °C for Ni [176] or Co [177] cations, and around 350 °C in the case of Fe [178]—whereas the major reduction occurred at higher temperatures, around 550–700 °C. The reduction range could be shifted, depending on chemical composition. For example, the presence of Mg cations shifted the temperature of the Ni reduction peak (on a temperature-programmed reduction profile) in Ni-doped chrysotile from 580 to 650–700 °C [179]. The reduction process was accompanied by the structural transformations of hydrosilicate, including dehydroxylation and the formation of metal silicate or crystalline SiO_2 in the high temperature range. Figure 39 shows Ni metal nanoparticles embedded in a residual nanotubular matrix [180]. The size of nanoparticles (NPs) also depended on the initial chemical composition, as well as on the reduction temperature and time. The typical Ni and Co NP size, that could be obtained with a 500 °C reduction, was around 5 nm [110,181]. At the same time, the SSA value of a metal/silicate composite could be preserved at a relatively high level of around 100 m^2/g. The metal NPs obtained by reduction are catalysts with a wide range of applications, including hydrogenation [176,177,182], the Fischer–Tropsch process [110], the water–gas shift reaction [179,183] and reforming [184–186]. The high stability and resistivity to the carbon deposition of these materials is considered to be a consequence of the strong coupling between metal NPs and the silicate matrix.

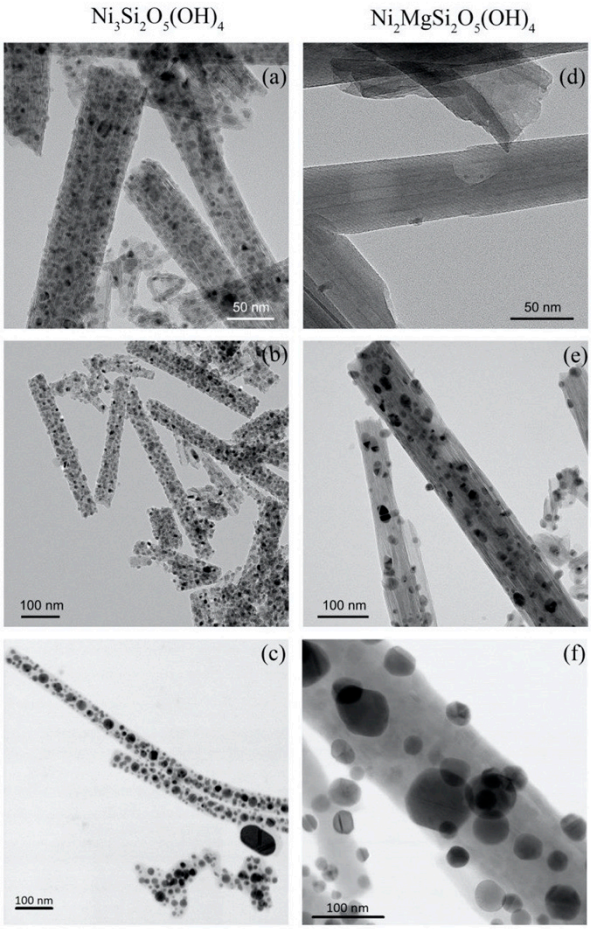

Figure 39. Electron micrographs of the nanoscrolls after annealing: (**a**–**c**) $Ni_3Si_2O_5(OH)_4$, (**d**–**f**) $Ni_2MgSi_2O_5(OH)_4$. Annealing temperatures: (**a**–**c**) 540, 670, 900 °C, respectively; (**d**–**f**) 400, 600, 900 °C, respectively, from [180].

Metal extraction from the nanotube structure is less abundant in the case of imogolite and halloysite. To the best of our knowledge, there have not been any attempts to reduce, for example, iron in Fe-doped imogolite, in spite of the synthesis of this material having been successful. However, halloysite is frequently used as a traditional catalyst in conjunction with a metal [187–191], an oxide [192–195] or another type of NP [196].

Furthermore, hydrosilicate nanotubes can be involved in a number of catalytic processes without preliminary reduction or decoration by NPs (although additional acid or heat treatment are still required). Heat-treated chrysotile has been successfully used for reforming benzene [197], biodiesel synthesis [198], esterification [199] and aldol condensation [200]. Bonelli et al. [201] demonstrated the acidic character of imogolite nanotubes and their performance in gas-phase phenol methylation. Ookawa [202] showed the catalytic activity of heat-treated imogolite in cyclohexane oxidation with H_2O_2. Halloysite nanotubes can be modified by sulfuric acid in order to strengthen their acidic properties [203] for use in the oligomerisation process.

5. Conclusions

Let us summarise some key points from this review: The modelling of hydrosilicate nanotubes enables a study of their morphology and of their mechanical and electronic properties. The preferred morphological parameters of single- and multi-walled chrysotile, halloysite and imogolite, as well as their cation doped derivatives, can be predicted as a function of strain, surface and adhesion energy.

Cation doping affects the size differences between the sheets and can change the direction of the scrolling. The lack of pure halloysite nanotubes synthesis reports suggests some hindrances; if these could be overcome, this should open a path for the synthesis of a number of halloysite-type scrolling hydrosilicates. Nanotubes' size can demonstrate nonlinear behaviour in relation to increases in guest cation concentration, because of the possible strain- and curvature-driven distribution of cations among, and within, single nanotubes. The formation of non-cylindrical morphologies also increases in the case of partial cation substitution. To date, the most significant impact of cation doped hydrosilicate nanotubes has occurred in the catalytic field. Other applications considered have generally involved pristine nanotubes. However, the cation doping approach can be fruitful for tuning the adsorption properties and mechanical response of hydrosilicate nanotubes.

Author Contributions: Conceptualisation, A.A.K.; writing—original draft preparation, A.A.K., E.K.K. and T.P.M.; writing—review and editing, E.K.K. and T.P.M.; visualisation, A.A.K.; supervision, A.A.K. All authors have read and agreed to the published version of the manuscript.

Funding: The research was supported by Russian Science Foundation Grant 16-13-10252.

Acknowledgments: The authors would like to thank V.V. Gusarov for fruitful discussions.

Conflicts of Interest: The authors declare no conflict of interest.

References

1. Pauling, L. The Structure of the Chlorites. *Proc. Natl. Acad. Sci. USA* **1930**, *16*, 578–582. [CrossRef]
2. Bowen, N.L.; Tuttle, O.F. The system MgO-SiO_2-H_2O. *Geol. Soc. Am. Bull.* **1949**, *60*, 439–460. [CrossRef]
3. Bates, T.F.; Hidebrand, F.A.; Swineford, A. Morphology and structure of endellite and halloysite. *Am. Mineral.* **1950**, *35*, 463–484.
4. Bates, T.F.; Sand, L.B.; Mink, J.F. Tubular crystals of chrysotile asbestos. *Science* **1950**, *111*, 512–513. [CrossRef] [PubMed]
5. Roy, D.M.; Roy, R. An experimental study of the formation and properties of synthetic serpentines and related layer silicate minerals. *Am. Mineral.* **1954**, *53*, 957–975.
6. Yang, J.C.-S. The growth of synthetic chrysotile fiber. *Am. Mineral.* **1961**, *46*, 748–752.
7. Saito, H.; Yamai, I. The Effect of Iron Ions on the Formation of Chrysotile under Hydrothermal-Dehydration Process. *J. Ceram. Assoc. Jpn.* **1968**, *76*, 331–337. [CrossRef]
8. Saito, H.; Yamai, I.; Kato, N. Conditions of Synthesis of Chrysotile Fibers under Hydrothermal-Dehydration Process. *J. Ceram. Assoc. Jpn.* **1968**, *76*, 247–253. [CrossRef]
9. Yada, K.; Iishi, K. Growth and microstructure of synthetic chrysotile. *Am. Mineral.* **1977**, *62*, 958–965.
10. Whittaker, E.J.W. The structure of chrysotile. II. Clino-chrysotile. *Acta Crystatllogr.* **1956**, *9*, 855–862. [CrossRef]
11. Whittaker, E.J.W. The structure of chrysotile. III. Ortho-chrysotile. *Acta Crystatllogr.* **1956**, *9*, 862–864. [CrossRef]
12. Whittaker, E.J.W. The structure of chrysotile. IV. Para-chrysotile. *Acta Crystatllogr.* **1956**, *9*, 865–867. [CrossRef]
13. Whittaker, E.J.W. The structure of chrysotile. V. Diffuse reflexions and fibre texture. *Acta Crystatllogr.* **1957**, *10*, 149–156. [CrossRef]
14. Yoshinaga, N.; Aomine, S. Imogolite in some ando soils. *Soil Sci. Plant Nutr.* **1962**, *8*, 22–29. [CrossRef]
15. Cradwick, P.D.G.; Farmer, V.C.; Russell, J.D.; Masson, C.R.; Wada, K.; Yoshinaga, N. Imogolite, a Hydrated Aluminium Silicate of Tubular Structure. *Nat. Phys. Sci.* **1972**, *240*, 187–189. [CrossRef]
16. Farmer, V.C.; Fraser, A.R.; Tait, J.M. Synthesis of imogolite: A tubular aluminium silicate polymer. *J. Chem. Soc. Chem. Commun.* **1977**, *12*, 462–463. [CrossRef]
17. Iijima, S. Helical microtubules of graphitic carbon. *Nature* **1991**, *354*, 56–58. [CrossRef]
18. Yuan, P.; Tan, D.; Annabi-Bergaya, F. Properties and applications of halloysite nanotubes: Recent research advances and future prospects. *Appl. Clay Sci.* **2015**, *112–113*, 75–93. [CrossRef]
19. Mellini, M.; Cressey, G.; Wicks, F.J.; Cressey, B.A. The crystal structure of Mg end-member lizardite-1T forming polyhedral spheres from the Lizard, Cornwall. *Mineral. Mag.* **2010**, *74*, 277–284. [CrossRef]
20. Weck, P.F.; Kim, E.; Jové-Colón, C.F. Relationship between crystal structure and thermo-mechanical properties of kaolinite clay: Beyond standard density functional theory. *Dalt. Trans.* **2015**, *44*, 12550–12560. [CrossRef]
21. Parfitt, R.L. Allophane and imogolite: Role in soil biogeochemical processes. *Clay Miner.* **2009**, *44*, 135–155. [CrossRef]

22. Thill, A.; Picot, P.; Belloni, L. A mechanism for the sphere/tube shape transition of nanoparticles with an imogolite local structure (imogolite and allophane). *Appl. Clay Sci.* **2017**, *141*, 308–315. [CrossRef]
23. Berthonneau, J.; Grauby, O.; Jeannin, C.; Chaudanson, D.; Joussein, E.; Baronnet, A. Native Morphology of Hydrated Spheroidal Halloysite Observed by Environmental Transmission Electron Microscopy. *Clays Clay Miner.* **2015**, *63*, 368–377. [CrossRef]
24. Cravero, F.; Fernández, L.; Marfil, S.; Sánchez, M.; Maiza, P.; Martínez, A. Spheroidal halloysites from Patagonia, Argentina: Some aspects of their formation and applications. *Appl. Clay Sci.* **2016**, *131*, 48–58. [CrossRef]
25. Chisholm, J.E. The number of sections in polygonal serpentine. *Can. Mineral.* **1992**, *30*, 355–365.
26. Cressey, B.A.; Whittaker, E.J.W. Five-Fold Symmetry in Chrysotile Asbestos Revealed by Transmission Electron Microscopy. *Mineral. Mag.* **1993**, *57*, 729–732. [CrossRef]
27. Dódony, I.; Buseck, P.R. Serpentines Close-Up and Intimate: An HRTEM View. *Int. Geol. Rev.* **2004**, *46*, 507–527. [CrossRef]
28. Sprynskyy, M.; Niedojadło, J.; Buszewski, B. Structural features of natural and acids modified chrysotile nanotubes. *J. Phys. Chem. Solids* **2011**, *72*, 1015–1026. [CrossRef]
29. Kato, K.; Inukai, K.; Fujikura, K.; Kasuga, T. Effective encapsulation of laccase in an aluminium silicate nanotube hydrogel. *New J. Chem.* **2014**, *38*, 3591–3599. [CrossRef]
30. Falini, G.; Foresti, E.; Gazzano, M.; Gualtieri, A.F.; Leoni, M.; Lesci, I.G.; Roveri, N. Tubular-shaped stoichiometric chrysotile nanocrystals. *Chemistry* **2004**, *10*, 3043–3049. [CrossRef]
31. Zhang, H.L.; Lei, X.R.; Yan, C.J.; Wang, H.Q.; Xiao, G.Q.; Hao, J.R.; Wang, D.; Qiu, X.M. Analysis on Crystal Structure of 7Å-Halloysite. *Adv. Mater. Res.* **2011**, *415–417*, 2206–2214. [CrossRef]
32. Demichelis, R.; Noël, Y.; D'Arco, P.; Maschio, L.; Orlando, R.; Dovesi, R. Structure and energetics of imogolite: A quantum mechanical ab initio study with B3LYP hybrid functional. *J. Mater. Chem.* **2010**, *20*, 10417. [CrossRef]
33. Mukherjee, S.; Bartlow, V.M.; Nair, S. Phenomenology of the Growth of Single-Walled Aluminosilicate and Aluminogermanate Nanotubes of Precise Dimensions. *Chem. Mater.* **2005**, *17*, 4900–4909. [CrossRef]
34. Alvarez-Ramírez, F. Ab initio simulation of the structural and electronic properties of aluminosilicate and aluminogermanate natotubes with imogolite-like structure. *Phys. Rev. B* **2007**, *76*, 125421. [CrossRef]
35. Saalfeld, H.; Wedde, M. Refinement of the crystal structure of gibbsite, $A1(OH)_3$. *Z. Krist. Cryst. Mater.* **1974**, *139*, 129–135. [CrossRef]
36. Downs, R.T.; Palmer, D.C. The pressure behavior of α cristobalite. *Am. Mineral.* **1994**, *79*, 9–14.
37. Desgranges, L.; Calvarin, G.; Chevrier, G. Interlayer interactions in $M(OH)_2$: A neutron diffraction study of $Mg(OH)_2$. *Acta Crystallogr. Sect. B Struct. Sci.* **1996**, *52*, 82–86. [CrossRef]
38. Krstanović, I. Crystal structure of single-layer lizardite. *Z. Krist. Cryst. Mater.* **1968**, *126*, 163–169. [CrossRef]
39. Momma, K.; Izumi, F. VESTA 3 for three-dimensional visualization of crystal, volumetric and morphology data. *J. Appl. Crystallogr.* **2011**, *44*, 1272–1276. [CrossRef]
40. Enyashin, A.N. Recent Advances in the Theory of Non-carbon Nanotubes. In *Computational Materials Discovery*; Oganov, A.R., Saleh, G., Eds.; Royal Society of Chemistry: Croydon, UK, 2018; pp. 352–391. ISBN 9781788010122.
41. Konduri, S.; Mukherjee, S.; Nair, S. Strain energy minimum and vibrational properties of single-walled aluminosilicate nanotubes. *Phys. Rev. B* **2006**, *74*, 033401. [CrossRef]
42. Guimarães, L.; Enyashin, A.N.; Frenzel, J.; Heine, T.; Duarte, H.A.; Seifert, G. Imogolite nanotubes: Stability, electronic, and mechanical properties. *ACS Nano* **2007**, *1*, 362–368. [CrossRef] [PubMed]
43. Lee, S.U.; Choi, Y.C.; Youm, S.G.; Sohn, D. Origin of the Strain Energy Minimum in Imogolite Nanotubes. *J. Phys. Chem. C* **2011**, *115*, 5226–5231. [CrossRef]
44. Alvarez-Ramírez, F. Theoretical Study of $(OH)_3N_2O_3MOH$, M = C, Si, Ge, Sn and N = Al, Ga, In, with Imogolite-Like Structure. *J. Comput. Theor. Nanosci.* **2009**, *6*, 1120–1124. [CrossRef]
45. Guimarães, L.; Pinto, Y.N.; Lourenço, M.P.; Duarte, H.A. Imogolite-like nanotubes: Structure, stability, electronic and mechanical properties of the phosphorous and arsenic derivatives. *Phys. Chem. Chem. Phys.* **2013**, *15*, 4303–4309. [CrossRef] [PubMed]
46. González, R.I.; Ramírez, R.; Rogan, J.; Valdivia, J.A.; Munoz, F.; Valencia, F.; Ramírez, M.; Kiwi, M. Model for Self-Rolling of an Aluminosilicate Sheet into a Single-Walled Imogolite Nanotube. *J. Phys. Chem. C* **2014**, *118*, 28227–28233. [CrossRef]

47. González, R.I.; Valencia, F.J.; Rogan, J.; Valdivia, J.A.; Sofo, J.; Kiwi, M.; Munoz, F. Bending energy of 2D materials: Graphene, MoS_2 and imogolite. *RSC Adv.* **2018**, *8*, 4577–4583. [CrossRef]
48. Poli, E.; Elliott, J.D.; Ratcliff, L.E.; Andrinopoulos, L.; Dziedzic, J.; Hine, N.D.M.; Mostofi, A.A.; Skylaris, C.-K.; Haynes, P.D.; Teobaldi, G. The potential of imogolite nanotubes as (co-)photocatalysts: A linear-scaling density functional theory study. *J. Phys. Condens. Matter* **2016**, *28*, 074003. [CrossRef]
49. Poli, E.; Elliott, J.D.; Chulkov, S.K.; Watkins, M.B.; Teobaldi, G. The Role of Cation-Vacancies for the Electronic and Optical Properties of Aluminosilicate Imogolite Nanotubes: A Non-local, Linear-Response TDDFT Study. *Front. Chem.* **2019**, *7*, 1–17. [CrossRef]
50. Liou, K.-H.; Tsou, N.-T.; Kang, D.-Y. Relationships among the structural topology, bond strength, and mechanical properties of single-walled aluminosilicate nanotubes. *Nanoscale* **2015**, *7*, 16222–16229. [CrossRef]
51. Liou, K.-H.; Kang, D.-Y. Defective Single-Walled Aluminosilicate Nanotubes: Structural Stability and Mechanical Properties. *ChemNanoMat* **2016**, *2*, 189–195. [CrossRef]
52. Liu, C.-H.; Kang, D.-Y. Influence of interwall interaction in double-walled aluminogermanate nanotubes on mechanical properties. *Comput. Mater. Sci.* **2017**, *135*, 54–63. [CrossRef]
53. Piperno, S.; Kaplan-Ashiri, I.; Cohen, S.R.; Popovitz-Biro, R.; Wagner, H.D.; Tenne, R.; Foresti, E.; Lesci, I.G.; Roveri, N. Characterization of Geoinspired and Synthetic Chrysotile Nanotubes by Atomic Force Microscopy and Transmission Electron Microscopy. *Adv. Funct. Mater.* **2007**, *17*, 3332–3338. [CrossRef]
54. Lecouvet, B.; Horion, J.; D'Haese, C.; Bailly, C.; Nysten, B. Elastic modulus of halloysite nanotubes. *Nanotechnology* **2013**, *24*, 105704. [CrossRef] [PubMed]
55. González, R.I.; Rogan, J.; Bringa, E.M.; Valdivia, J.A. Mechanical Response of Aluminosilicate Nanotubes under Compression. *J. Phys. Chem. C* **2016**, *120*, 14428–14434. [CrossRef]
56. Guimarães, L.; Enyashin, A.N.; Seifert, G.; Duarte, H.A. Structural, Electronic, and Mechanical Properties of Single-Walled Halloysite Nanotube Models. *J. Phys. Chem. C* **2010**, *114*, 11358–11363. [CrossRef]
57. Lourenço, M.P.; de Oliveira, C.; Oliveira, A.F.; Guimarães, L.; Duarte, H.A. Structural, Electronic, and Mechanical Properties of Single-Walled Chrysotile Nanotube Models. *J. Phys. Chem. C* **2012**, *116*, 9405–9411. [CrossRef]
58. Demichelis, R.; De La Pierre, M.; Mookherjee, M.; Zicovich-Wilson, C.M.; Orlando, R. Serpentine polymorphism: A quantitative insight from first-principles calculations. *CrystEngComm* **2016**, *18*, 4412–4419. [CrossRef]
59. Ferrante, F.; Armata, N.; Lazzara, G. Modeling of the Halloysite Spiral Nanotube. *J. Phys. Chem. C* **2015**, *119*, 16700–16707. [CrossRef]
60. Prishchenko, D.A.; Zenkov, E.V.; Mazurenko, V.V.; Fakhrullin, R.F.; Lvov, Y.M.; Mazurenko, V.G. Molecular dynamics of the halloysite nanotubes. *Phys. Chem. Chem. Phys.* **2018**, *20*, 5841–5849. [CrossRef]
61. Alvarez-Ramírez, F.; Toledo-Antonio, J.A.; Angeles-Chavez, C.; Guerrero-Abreo, J.H.; López-Salinas, E. Complete Structural Characterization of $Ni_3Si_2O_5(OH)_4$ Nanotubes: Theoretical and Experimental Comparison. *J. Phys. Chem. C* **2011**, *115*, 11442–11446. [CrossRef]
62. Fu, L.; Yang, H. Structure and Electronic Properties of Transition Metal Doped Kaolinite Nanoclay. *Nanoscale Res. Lett.* **2017**, *12*, 411. [CrossRef] [PubMed]
63. Singh, B. Why Does Halloysite Roll?—A New Model. *Clays Clay Miner.* **1996**, *44*, 191–196. [CrossRef]
64. Perbost, R.; Amouric, M.; Olives, J. Influence of Cation Size on the Curvature of Serpentine Minerals: HRTEM-AEM Study and Elastic Theory. *Clays Clay Miner.* **2003**, *51*, 430–438. [CrossRef]
65. Thill, A.; Guiose, B.; Bacia-Verloop, M.; Geertsen, V.; Belloni, L. How the Diameter and Structure of $(OH)_3Al_2O_3Si_xGe_{1-x}OH$ Imogolite Nanotubes Are Controlled by an Adhesion versus Curvature Competition. *J. Phys. Chem. C* **2012**, *116*, 26841–26849. [CrossRef]
66. Thill, A.; Maillet, P.; Guiose, B.; Spalla, O.; Belloni, L.; Chaurand, P.; Auffan, M.; Olivi, L.; Rose, J. Physico-chemical Control over the Single- or Double-Wall Structure of Aluminogermanate Imogolite-like Nanotubes. *J. Am. Chem. Soc.* **2012**, *134*, 3780–3786. [CrossRef]
67. Chivilikhin, S.A.; Popov, I.Y.; Blinova, I.V.; Kirillova, S.A.; Konovalov, A.S.; Oblogin, S.I.; Tishkin, V.O.; Chernov, I.A.; Gusarov, V.V. Simulation of the formation of nanorolls. *Glass Phys. Chem.* **2007**, *33*, 315–319. [CrossRef]
68. Chivilikhin, S.A.; Popov, I.Y.; Svitenkov, A.I.; Chivilikhin, D.S.; Gusarov, V.V. Formation and evolution of nanoscroll ensembles based on layered-structure compounds. *Dokl. Phys.* **2009**, *54*, 491–493. [CrossRef]

69. Maillet, P.; Levard, C.; Spalla, O.; Masion, A.; Rose, J.; Thill, A. Growth kinetic of single and double-walled aluminogermanate imogolite-like nanotubes: An experimental and modeling approach. *Phys. Chem. Chem. Phys.* **2011**, *13*, 2682–2689. [CrossRef]
70. Yucelen, G.I.; Kang, D.-Y.; Schmidt-Krey, I.; Beckham, H.W.; Nair, S. A generalized kinetic model for the formation and growth of single-walled metal oxide nanotubes. *Chem. Eng. Sci.* **2013**, *90*, 200–212. [CrossRef]
71. Krasilin, A.A.; Gusarov, V.V. Energy of formation of chrysotile nanotubes. *Russ. J. Gen. Chem.* **2014**, *84*, 2359–2363. [CrossRef]
72. Prinz, V.Y. A new concept in fabricating building blocks for nanoelectronic and nanomechanic devices. *Microelectron. Eng.* **2003**, *69*, 466–475. [CrossRef]
73. Mutilin, S.V.; Soots, R.A.; Vorob'ev, A.B.; Ikusov, D.G.; Mikhailov, N.N.; Prinz, V.Y. Microtubes and corrugations fabricated from strained ZnTe/CdHgTe/HgTe/CdHgTe heterofilms with 2D electron–hole gas in the HgTe quantum well. *J. Phys. D Appl. Phys.* **2014**, *47*, 295301. [CrossRef]
74. Gulina, L.B.; Tolstoy, V.P.; Petrov, Y.V.; Danilov, D.V. Interface-Assisted Synthesis of Single-Crystalline ScF_3 Microtubes. *Inorg. Chem.* **2018**, *57*, 9779–9781. [CrossRef] [PubMed]
75. Chizmeshya, A.V.G.; McKelvy, M.J.; Sharma, R.; Carpenter, R.W.; Bearat, H. Density functional theory study of the decomposition of $Mg(OH)_2$: A lamellar dehydroxylation model. *Mater. Chem. Phys.* **2003**, *77*, 416–425. [CrossRef]
76. Krasilin, A.A.; Nevedomsky, V.N.; Gusarov, V.V. Comparative Energy Modeling of Multiwalled $Mg_3Si_2O_5(OH)_4$ and $Ni_3Si_2O_5(OH)_4$ Nanoscroll Growth. *J. Phys. Chem. C* **2017**, *121*, 12495–12502. [CrossRef]
77. Krasilin, A.A. Energy modeling of competition between tubular and platy morphologies of chrysotile and halloysite layers. *Clays Clay Miner.* accepted. [CrossRef]
78. Shchipalov, Y.K. Surface Energy of Crystalline and Vitreous Silica. *Glass Ceram.* **2000**, *57*, 374–377. [CrossRef]
79. Churakov, S.V.; Iannuzzi, M.; Parrinello, M. Ab Initio Study of Dehydroxylation−Carbonation Reaction on Brucite Surface. *J. Phys. Chem. B* **2004**, *108*, 11567–11574. [CrossRef]
80. Fleming, S.; Rohl, A.; Lee, M.-Y.; Gale, J.; Parkinson, G. Atomistic modelling of gibbsite: Surface structure and morphology. *J. Cryst. Growth* **2000**, *209*, 159–166. [CrossRef]
81. Evarestov, R.A.; Bandura, A.V. HF and DFT calculations of MgO surface energy and electrostatic potential using two- and three-periodic models. *Int. J. Quantum Chem.* **2004**, *100*, 452–459. [CrossRef]
82. Krasilin, A.A.; Gusarov, V.V. Energy model of bilayer nanoplate scrolling: Formation of chrysotile nanoscroll. *Russ. J. Gen. Chem.* **2015**, *85*, 2238–2241. [CrossRef]
83. Krasilin, A.A.; Gusarov, V.V. Energy Model of Radial Growth of a Nanotubular Crystal. *Tech. Phys. Lett.* **2016**, *42*, 55–58. [CrossRef]
84. Tolman, R.C. The Effect of Droplet Size on Surface Tension. *J. Chem. Phys.* **1949**, *17*, 333. [CrossRef]
85. Vollath, D.; Fischer, F.D.; Holec, D. Surface energy of nanoparticles—Influence of particle size and structure. *Beilstein J. Nanotechnol.* **2018**, *9*, 2265–2276. [CrossRef]
86. Wendler, K.; Thar, J.; Zahn, S.; Kirchner, B. Estimating the Hydrogen Bond Energy. *J. Phys. Chem. A* **2010**, *114*, 9529–9536. [CrossRef]
87. Ramesh, T.N.; Kamath, P.V.; Shivakumara, C. Classification of stacking faults and their stepwise elimination during the disorder → order transformation of nickel hydroxide. *Acta Crystallogr. Sect. B Struct. Sci.* **2006**, *62*, 530–536. [CrossRef]
88. Koza, J.A.; Hull, C.M.; Liu, Y.-C.; Switzer, J.A. Deposition of β-$Co(OH)_2$ Films by Electrochemical Reduction of Tris(ethylenediamine)cobalt(III) in Alkaline Solution. *Chem. Mater.* **2013**, *25*, 1922–1926. [CrossRef]
89. Wyckoff, R.W.G. *Crystal Structures*, 2nd ed.; Interscience Publishers: New York, NY, USA, 1963; Volume 1, p. 467.
90. Smith, G.S.; Isaacs, P.B. The crystal structure of quartz-like GeO_2. *Acta Crystallogr.* **1964**, *17*, 842–846. [CrossRef]
91. Lacks, D.J.; Gordon, R.G. Crystal-structure calculations with distorted ions. *Phys. Rev. B* **1993**, *48*, 2889–2908. [CrossRef]
92. Deliens, M.; Goethals, H. Polytypism of heterogenite. *Mineral. Mag.* **1973**, *39*, 152–157. [CrossRef]
93. Urusov, V.S. The phenomenological theory of solid solutions. *Solid Solut. Silic. Oxide Syst.* **2001**, *3*, 121–153. [CrossRef]
94. Shannon, R.D.; Prewitt, C.T. Effective ionic radii in oxides and fluorides. *Acta Crystallogr. Sect. B Struct. Crystallogr. Cryst. Chem.* **1969**, *25*, 925–946. [CrossRef]

95. Maillet, P.; Levard, C.; Larquet, E.; Mariet, C.; Spalla, O.; Menguy, N.; Masion, A.; Doelsch, E.; Rose, J.; Thill, A. Evidence of double-walled Al-Ge imogolite-like nanotubes. A cryo-TEM and SAXS investigation. *J. Am. Chem. Soc.* **2010**, *132*, 1208–1209. [CrossRef] [PubMed]
96. Krasilin, A.A.; Khrapova, E.K. Effect of hydrothermal treatment conditions on formation of nickel hydrogermanate with platy morphology. *Russ. J. Appl. Chem.* **2017**, *90*, 22–27. [CrossRef]
97. White, R.D.; Bavykin, D.V.; Walsh, F.C. Spontaneous Scrolling of Kaolinite Nanosheets into Halloysite Nanotubes in an Aqueous Suspension in the Presence of GeO_2. *J. Phys. Chem. C* **2012**, *116*, 8824–8833. [CrossRef]
98. Landau, L.D.; Lifshitz, E.M. *Statistical Physics*, 3rd ed.; Elsevier Butterworth-Heinemann: Oxford, UK, 1980; Volume 5, p. 544. ISBN 9780080570464.
99. Almjasheva, O.V.; Krasilin, A.A.; Gusarov, V.V. Formation mechanism of core-shell nanocrystals obtained via dehydration of coprecipitated hydroxides at hydrothermal conditions. *Nanosyst. Phys. Chem. Math.* **2018**, *9*, 568–572. [CrossRef]
100. Bloise, A.; Barrese, E.; Apollaro, C. Hydrothermal alteration of Ti-doped forsterite to chrysotile and characterization of the resulting chrysotile fibers. *Neues Jahrb. Mineral. Abh.* **2009**, *185*, 297–304. [CrossRef]
101. Maslennikova, T.P.; Gatina, E.N. Hydrothermal Synthesis of Ti-Doped Nickel Hydrosilicates of Various Morphologies. *Russ. J. Appl. Chem.* **2018**, *91*, 286–291. [CrossRef]
102. Korytkova, E.N.; Pivovarova, L.N.; Semenova, O.E.; Drozdova, I.A.; Povinich, V.F.; Gusarov, V.V. Hydrothermal synthesis of nanotubular Mg-Fe hydrosilicate. *Russ. J. Inorg. Chem.* **2007**, *52*, 338–344. [CrossRef]
103. Bloise, A.; Belluso, E.; Barrese, E.; Miriello, D.; Apollaro, C. Synthesis of Fe-doped chrysotile and characterization of the resulting chrysotile fibers. *Cryst. Res. Technol.* **2009**, *44*, 590–596. [CrossRef]
104. Krasilin, A.A.; Suprun, A.M.; Gusarov, V.V. Influence of Component Ratio in the Compound $(Mg,Fe)_3Si_2O_5(OH)_4$ on the Formation of Nanotubular and Platelike Particles. *Russ. J. Appl. Chem.* **2013**, *86*, 1633–1637. [CrossRef]
105. Krasilin, A.A.; Panchuk, V.V.; Semenov, V.G.; Gusarov, V.V. Formation of Variable-Composition Iron(III) Hydrosilicates with the Chrysotile Structure. *Russ. J. Gen. Chem.* **2016**, *86*, 2581–2588. [CrossRef]
106. Borghi, E.; Occhiuzzi, M.; Foresti, E.; Lesci, I.G.; Roveri, N. Spectroscopic characterization of Fe-doped synthetic chrysotile by EPR, DRS and magnetic susceptibility measurements. *Phys. Chem. Chem. Phys.* **2010**, *12*, 227–238. [CrossRef] [PubMed]
107. Shafia, E.; Esposito, S.; Manzoli, M.; Chiesa, M.; Tiberto, P.; Barrera, G.; Menard, G.; Allia, P.; Freyria, F.S.; Garrone, E.; et al. Al/Fe isomorphic substitution versus Fe_2O_3 clusters formation in Fe-doped aluminosilicate nanotubes (imogolite). *J. Nanopart. Res.* **2015**, *17*, 336. [CrossRef]
108. Shafia, E.; Esposito, S.; Armandi, M.; Manzoli, M.; Garrone, E.; Bonelli, B. Isomorphic substitution of aluminium by iron into single-walled alumino-silicate nanotubes: A physico-chemical insight into the structural and adsorption properties of Fe-doped imogolite. *Microporous Mesoporous Mater.* **2016**, *224*, 229–238. [CrossRef]
109. Korytkova, E.N.; Pivovarova, L.N.; Drosdova, I.A.; Gusarov, V.V. Hydrothermal synthesis of nanotubular Co-Mg hydrosilicates with the chrysotile structure. *Russ. J. Gen. Chem.* **2007**, *77*, 1669–1676. [CrossRef]
110. Park, J.C.; Kang, S.W.; Kim, J.-C.; Kwon, J.I.; Jang, S.; Rhim, G.B.; Kim, M.; Chun, D.H.; Lee, H.-T.; Jung, H.; et al. Synthesis of Co/SiO_2 hybrid nanocatalyst via twisted $Co_3Si_2O_5(OH)_4$ nanosheets for high-temperature Fischer–Tropsch reaction. *Nano Res.* **2017**, *10*, 1044–1055. [CrossRef]
111. Korytkova, E.N.; Maslov, A.V.; Pivovarova, L.N.; Polegotchenkova, Y.V.; Povinich, V.F.; Gusarov, V.V. Synthesis of Nanotubular $Mg_3Si_2O_5(OH)_4$-$Ni_3Si_2O_5(OH)_4$ Silicates at Elevated Temperatures and Pressures. *Inorg. Mater.* **2005**, *41*, 743–749. [CrossRef]
112. McDonald, A.; Scott, B.; Villemure, G. Hydrothermal preparation of nanotubular particles of a 1:1 nickel phyllosilicate. *Microporous Mesoporous Mater.* **2009**, *120*, 263–266. [CrossRef]
113. White, R.D.; Bavykin, D.V.; Walsh, F.C. Morphological control of synthetic $Ni_3Si_2O_5(OH)_4$ nanotubes in an alkaline hydrothermal environment. *J. Mater. Chem. A* **2013**, *1*, 548–556. [CrossRef]
114. Krasilin, A.A.; Semenova, A.S.; Kellerman, D.G.; Nevedomsky, V.N.; Gusarov, V.V. Magnetic properties of synthetic $Ni_3Si_2O_5(OH)_4$ nanotubes. *EPL (Europhys. Lett.)* **2016**, *113*, 47006. [CrossRef]
115. Bloise, A.; Belluso, E.; Fornero, E.; Rinaudo, C.; Barrese, E.; Capella, S. Influence of synthesis conditions on growth of Ni-doped chrysotile. *Microporous Mesoporous Mater.* **2010**, *132*, 239–245. [CrossRef]

116. Krasilin, A.A.; Suprun, A.M.; Nevedomsky, V.N.; Gusarov, V.V. Formation of Conical $(Mg,Ni)_3Si_2O_5(OH)_4$ Nanoscrolls. *Dokl. Phys. Chem.* **2015**, *460*, 42–44. [CrossRef]
117. Krasilin, A.A.; Gusarov, V.V. Redistribution of Mg and Ni cations in crystal lattice of conical nanotube with chrysotile structure. *Nanosyst. Phys. Chem. Math.* **2017**, *8*, 620–627. [CrossRef]
118. Krasilin, A.A.; Khrapova, E.K.; Nominé, A.; Ghanbaja, J.; Belmonte, T.; Gusarov, V.V. Cation Redistribution along the Spiral of Ni-Doped Phyllosilicate Nanoscrolls: Energy Modelling and STEM/EDS Study. *ChemPhysChem* **2019**, *20*, 719–726. [CrossRef]
119. Krasilin, A.A.; Suprun, A.M.; Ubyivovk, E.V.; Gusarov, V.V. Morphology vs. chemical composition of single Ni-doped hydrosilicate nanoscroll. *Mater. Lett.* **2016**, *171*, 68–71. [CrossRef]
120. Korytkova, E.N.; Brovkin, A.S.; Maslennikova, T.P.; Pivovarova, L.N.; Drozdova, I.A. Influence of the Physicochemical Parameters of Synthesis on the Growth of Nanotubes of the $Mg_3Si_2O_5(OH)_4$ Composition under Hydrothermal Conditions. *Glass Phys. Chem.* **2011**, *37*, 161–171. [CrossRef]
121. Baronnet, A.; Mellini, M.; Devouard, B. Sectors in polygonal serpentine. A model based on dislocations. *Phys. Chem. Miner.* **1994**, *21*, 330–343. [CrossRef]
122. Cressey, G.; Cressey, B.A.; Wicks, F.J.; Yada, K. A disc with fivefold symmetry: The proposed fundamental seed structure for the formation of chrysotile asbestos fibres, polygonal serpentine fibres and polyhedral lizardite spheres. *Mineral. Mag.* **2010**, *74*, 29–37. [CrossRef]
123. Devouard, B.; Baronnet, A.; Van Tendeloo, G.; Amelinckx, S. First evidence of synthetic polygonal serpentines. *Eur. J. Mineral.* **1997**, *9*, 539–546. [CrossRef]
124. Krasilin, A.A.; Gusarov, V.V. Control over morphology of magnesium-aluminum hydrosilicate nanoscrolls. *Russ. J. Appl. Chem.* **2015**, *88*, 1928–1935. [CrossRef]
125. Amara, M.-S.; Paineau, E.; Bacia-Verloop, M.; Krapf, M.-E.M.; Davidson, P.; Belloni, L.; Levard, C.; Rose, J.; Launois, P.; Thill, A. Single-step formation of micron long $(OH)_3Al_2O_3Ge(OH)$ imogolite-like nanotubes. *Chem. Commun.* **2013**, *49*, 11284–11286. [CrossRef] [PubMed]
126. Paineau, E. Imogolite Nanotubes: A Flexible Nanoplatform with Multipurpose Applications. *Appl. Sci.* **2018**, *8*, 1921. [CrossRef]
127. Zhang, A.B.; Pan, L.; Zhang, H.Y.; Liu, S.T.; Ye, Y.; Xia, M.S.; Chen, X.G. Effects of acid treatment on the physico-chemical and pore characteristics of halloysite. *Colloids Surf. A Physicochem. Eng. Asp.* **2012**, *396*, 182–188. [CrossRef]
128. Shu, Z.; Chen, Y.; Zhou, J.; Li, T.; Yu, D.; Wang, Y. Nanoporous-walled silica and alumina nanotubes derived from halloysite: Controllable preparation and their dye adsorption applications. *Appl. Clay Sci.* **2015**, *112–113*, 17–24. [CrossRef]
129. Deng, L.; Yuan, P.; Liu, D.; Du, P.; Zhou, J.; Wei, Y.; Song, Y.; Liu, Y. Effects of calcination and acid treatment on improving benzene adsorption performance of halloysite. *Appl. Clay Sci.* **2019**, *181*, 105240. [CrossRef]
130. Yucelen, G.I.; Kang, D.-Y.; Guerrero-Ferreira, R.C.; Wright, E.R.; Beckham, H.W.; Nair, S. Shaping single-walled metal oxide nanotubes from precursors of controlled curvature. *Nano Lett.* **2012**, *12*, 827–832. [CrossRef]
131. Maslennikova, T.P.; Korytkova, E.N. Influence of Synthesis of Physicochemical Parameters on Growth of $Ni_3Si_2O_5(OH)_4$ Nanotubes and Their Filling with Solutions of Hydroxides and Chlorides of Alkaline Metals. *Glass Phys. Chem.* **2013**, *39*, 67–72. [CrossRef]
132. Ackerman, W.C.; Smith, D.M.; Huling, J.C.; Kim, Y.W.; Bailey, J.K.; Brinker, C.J. Gas/vapor adsorption in imogolite: A microporous tubular aluminosilicate. *Langmuir* **1993**, *9*, 1051–1057. [CrossRef]
133. Ohashi, F.; Tomura, S.; Akaku, K.; Hayashi, S.; Wada, S.-I. Characterization of synthetic imogolite nanotubes as gas storage. *J. Mater. Sci.* **2004**, *39*, 1799–1801. [CrossRef]
134. Bottero, I.; Bonelli, B.; Ashbrook, S.E.; Wright, P.A.; Zhou, W.; Tagliabue, M.; Armandi, M.; Garrone, E. Synthesis and characterization of hybrid organic/inorganic nanotubes of the imogolite type and their behaviour towards methane adsorption. *Phys. Chem. Chem. Phys.* **2011**, *13*, 744–750. [CrossRef] [PubMed]
135. Vitillo, J.G. Magnesium-based systems for carbon dioxide capture, storage and recycling: From leaves to synthetic nanostructured materials. *RSC Adv.* **2015**, *5*, 36192–36239. [CrossRef]
136. Krasilin, A.A.; Danilovich, D.P.; Yudina, E.B.; Bruyere, S.; Ghanbaja, J.; Ivanov, V.K. Crystal violet adsorption by oppositely twisted heat-treated halloysite and pecoraite nanoscrolls. *Appl. Clay Sci.* **2019**, *173*, 1–11. [CrossRef]
137. Cavallaro, G.; Lazzara, G.; Milioto, S.; Parisi, F. Hydrophobically Modified Halloysite Nanotubes as Reverse Micelles for Water-in-Oil Emulsion. *Langmuir* **2015**, *31*, 7472–7478. [CrossRef]

138. Valentim, I.B.; Joekes, I. Adsorption of sodium dodecylsulfate on chrysotile. *Colloids Surf. A Physicochem. Eng. Asp.* **2006**, *290*, 106–111. [CrossRef]
139. Bonini, M.; Gabbani, A.; Del Buffa, S.; Ridi, F.; Baglioni, P.; Bordes, R.; Holmberg, K. Adsorption of Amino Acids and Glutamic Acid-Based Surfactants on Imogolite Clays. *Langmuir* **2017**, *33*, 2411–2419. [CrossRef]
140. Lo Dico, G.; Semilia, F.; Milioto, S.; Parisi, F.; Cavallaro, G.; Inguì, G.; Makaremi, M.; Pasbakhsh, P.; Lazzara, G. Microemulsion Encapsulated into Halloysite Nanotubes and their Applications for Cleaning of a Marble Surface. *Appl. Sci.* **2018**, *8*, 1455. [CrossRef]
141. Yu, S.; Zhai, L.; Wang, Y.; Liu, X.; Xu, L.; Cheng, L. Synthesis of magnetic chrysotile nanotubes for adsorption of Pb(II), Cd(II) and Cr(III) ions from aqueous solution. *J. Environ. Chem. Eng.* **2015**, *3*, 752–762. [CrossRef]
142. Cheng, L.; Yu, S.; Zha, C.; Yao, Y.; Pan, X. Removal of simulated radionuclide Ce(III) from aqueous solution by as-synthesized chrysotile nanotubes. *Chem. Eng. J.* **2012**, *213*, 22–30. [CrossRef]
143. Chiew, C.S.C.; Yeoh, H.K.; Pasbakhsh, P.; Poh, P.E.; Tey, B.T.; Chan, E.S. Stability and reusability of alginate-based adsorbents for repetitive lead (II) removal. *Polym. Degrad. Stab.* **2016**, *123*, 146–154. [CrossRef]
144. Liou, K.-H.; Kang, D.-Y.; Lin, L.-C. Investigating the Potential of Single-Walled Aluminosilicate Nanotubes in Water Desalination. *ChemPhysChem* **2017**, *18*, 179–183. [CrossRef] [PubMed]
145. Cheng, L.L.; Wei, X.D.; Hao, X.L.; Ruan, D.; Yu, S.M. The removal of strontium(II) and neodymium(III) from their aqueous solutions on chrysotile nanotubes. *Adv. Mater. Res.* **2014**, *881–883*, 519–524. [CrossRef]
146. Maslennikova, T.P.; Korytkova, E.N. Aqueous Solutions of Cesium Salts and Cesium Hydroxide in Hydrosilicate Nanotubes of the $Mg_3Si_2O_5(OH)_4$ Composition. *Glass Phys. Chem.* **2010**, *36*, 345–350. [CrossRef]
147. Maslennikova, T.P.; Korytkova, E.N. Regularities of the Filling of $Mg_3Si_2O_5(OH)_4$ Hydrosilicate Nanotubes with Solutions of Sodium Hydroxide and Sodium Chloride. *Glass Phys. Chem.* **2011**, *37*, 418–425. [CrossRef]
148. Saki, H.; Alemayehu, E.; Schomburg, J.; Lennartz, B. Halloysite nanotubes as adsorptive material for phosphate removal from aqueous solution. *Water* **2019**, *11*, 203. [CrossRef]
149. Shu, Z.; Chen, Y.; Zhou, J.; Li, T.; Sheng, Z.; Tao, C.; Wang, Y. Preparation of halloysite-derived mesoporous silica nanotube with enlarged specific surface area for enhanced dye adsorption. *Appl. Clay Sci.* **2016**, *132–133*, 114–121. [CrossRef]
150. Peng, Q.; Liu, M.; Zheng, J.; Zhou, C. Adsorption of dyes in aqueous solutions by chitosan–halloysite nanotubes composite hydrogel beads. *Microporous Mesoporous Mater.* **2015**, *201*, 190–201. [CrossRef]
151. Cavallaro, G.; Milioto, S.; Lazzara, G. Halloysite Nanotubes: Interfacial Properties and Applications in Cultural Heritage. *Langmuir* **2020**, *36*, 3677–3689. [CrossRef]
152. Cavallaro, G.; Milioto, S.; Konnova, S.A.; Fakhrullina, G.; Akhatova, F.; Lazzara, G.; Fakhrullin, R.F.; Lvov, Y. Halloysite/keratin nanocomposite for human hair photoprotection coating. *ACS Appl. Mater. Interfaces* **2020**, *12*, 24348–24362. [CrossRef]
153. Falcón, J.M.; Sawczen, T.; Aoki, I.V. Dodecylamine-Loaded Halloysite Nanocontainers for Active Anticorrosion Coatings. *Front. Mater.* **2015**, *2*, 69. [CrossRef]
154. Zahidah, K.A.; Kakooei, S.; Ismail, M.C.; Raja, P.B. Halloysite nanotubes as nanocontainer for smart coating application: A review. *Prog. Org. Coat.* **2017**, *111*, 175–185. [CrossRef]
155. Mahmoudi, R.; Kardar, P.; Arabi, A.M.; Amini, R.; Pasbakhsh, P. The active corrosion performance of silane coating treated by praseodymium encapsulated with halloysite nanotubes. *Prog. Org. Coat.* **2020**, *138*, 105404. [CrossRef]
156. Jin, X.; Zhang, R.; Su, M.; Li, H.; Yue, X.; Qin, D.; Jiang, Z. Functionalization of halloysite nanotubes by enlargement and layer-by-layer assembly for controlled release of the fungicide iodopropynyl butylcarbamate. *RSC Adv.* **2019**, *9*, 42062–42070. [CrossRef]
157. Patel, S.; Jammalamadaka, U.; Sun, L.; Tappa, K.; Mills, D. Sustained Release of Antibacterial Agents from Doped Halloysite Nanotubes. *Bioengineering* **2015**, *3*, 1. [CrossRef] [PubMed]
158. Stavitskaya, A.; Batasheva, S.; Vinokurov, V.; Fakhrullina, G.; Sangarov, V.; Lvov, Y.; Fakhrullin, R. Antimicrobial Applications of Clay Nanotube-Based Composites. *Nanomaterials* **2019**, *9*, 708. [CrossRef]
159. Santos, A.C.; Ferreira, C.; Veiga, F.; Ribeiro, A.J.; Panchal, A.; Lvov, Y.; Agarwal, A. Halloysite clay nanotubes for life sciences applications: From drug encapsulation to bioscaffold. *Adv. Colloid Interface Sci.* **2018**, *257*, 58–70. [CrossRef]

160. Liu, M.; Chang, Y.; Yang, J.; You, Y.; He, R.; Chen, T.; Zhou, C. Functionalized halloysite nanotube by chitosan grafting for drug delivery of curcumin to achieve enhanced anticancer efficacy. *J. Mater. Chem. B* **2016**, *4*, 2253–2263. [CrossRef]
161. Bediako, E.G.; Nyankson, E.; Dodoo-Arhin, D.; Agyei-Tuffour, B.; Łukowiec, D.; Tomiczek, B.; Yaya, A.; Efavi, J.K. Modified halloysite nanoclay as a vehicle for sustained drug delivery. *Heliyon* **2018**, *4*, e00389. [CrossRef]
162. Fizir, M.; Dramou, P.; Dahiru, N.S.; Ruya, W.; Huang, T.; He, H. Halloysite nanotubes in analytical sciences and in drug delivery: A review. *Microchim. Acta* **2018**, *185*, 389. [CrossRef]
163. Lvov, Y.M.; DeVilliers, M.M.; Fakhrullin, R.F. The application of halloysite tubule nanoclay in drug delivery. *Expert Opin. Drug Deliv.* **2016**, *13*, 977–986. [CrossRef]
164. Stan, G.; Ciobanu, C.V.; Parthangal, P.M.; Cook, R.F. Diameter-Dependent Radial and Tangential Elastic Moduli of ZnO Nanowires. *Nano Lett.* **2007**, *7*, 3691–3697. [CrossRef]
165. Lawrence, J.G.; Berkan, L.M.; Nadarajah, A. Elastic properties and morphology of individual carbon nanofibers. *ACS Nano* **2008**, *2*, 1230–1236. [CrossRef] [PubMed]
166. Krasilin, A.A.; Suprun, A.M.; Ubyivovk, E.V.; Nevedomsky, V.N.; Scherbin, B.O.; Petrov, A.A. Interconnection between composition, morphology and mechanics of chrysotile nanoscroll. In Proceedings of the Multinational Congress on Microscopy MCM 2015, Eger, Hungary, 23–28 August 2015; pp. 459–460.
167. Ankudinov, A.V. On the accuracy of the probe-sample contact stiffness measured by an atomic force microscope. *Nanosyst. Phys. Chem. Math.* **2019**, *10*, 642–653. [CrossRef]
168. Yah, W.O.; Yamamoto, K.; Jiravanichanun, N.; Otsuka, H.; Takahara, A. Imogolite Reinforced Nanocomposites: Multifaceted Green Materials. *Materials* **2010**, *3*, 1709–1745. [CrossRef]
169. Gaaz, T.; Sulong, A.; Kadhum, A.; Al-Amiery, A.; Nassir, M.; Jaaz, A. The Impact of Halloysite on the Thermo-Mechanical Properties of Polymer Composites. *Molecules* **2017**, *22*, 838. [CrossRef]
170. Jiang, Y.; Wang, P.; Zheng, J. Use of ionic monomers to prepare halloysite polymer nanocomposites with reinforced mechanical performance. *Appl. Clay Sci.* **2017**, *141*, 248–256. [CrossRef]
171. Dobrovol'skaya, I.P.; Popryadukhin, P.V.; Khomenko, A.Y.; Dresvyanina, E.N.; Yudin, V.E.; Elokhovskii, V.Y.; Chvalun, S.N.; Saprykina, N.N.; Maslennikova, T.P.; Korytkova, E.N. Structure and characteristics of chitosan-based fibers containing chrysotile and halloysite. *Polym. Sci. Ser. A* **2011**, *53*, 418–423. [CrossRef]
172. Wu, Y.; Yudin, V.E.; Otaigbe, J.U.; Korytkova, E.N.; Nazarenko, S. Gas barrier behavior of polyimide films filled with synthetic chrysotile nanotubes. *J. Polym. Sci. Part B Polym. Phys.* **2013**, *51*, 1184–1193. [CrossRef]
173. Rall, J.D.; Seehra, M.S. The nature of the magnetism in quasi-2D layered α-$Ni(OH)_2$. *J. Phys. Condens. Matter* **2012**, *24*, 076002. [CrossRef]
174. Miyamoto, H. The Magnetic Properties of $Fe(OH)_2$. *Mater. Res. Bull.* **1976**, *11*, 329–335. [CrossRef]
175. Yang, Y.; Liang, Q.; Li, J.; Zhuang, Y.; He, Y.; Bai, B.; Wang, X. $Ni_3Si_2O_5(OH)_4$ Multi-Walled Nanotubes with Tunable Magnetic Properties and Their Application as Anode Materials for Lithium Batteries. *Nano Res.* **2011**, *4*, 882–890. [CrossRef]
176. Nitta, Y.; Kawabe, M.; Sun, L.; Ohmachi, Y.; Imanaka, T. Preparation of uniformly dispersed nickel/silica catalysts from synthetic nickel-chrysotile. *Appl. Catal.* **1989**, *53*, 15–28. [CrossRef]
177. Nitta, Y.; Ueno, K.; Imanaka, T. Selective Hydrogenation of α,β-Unsaturated Aldehydes on Cobalt-Silica Catalysts Obtained from Cobalt Chrysotile. *Appl. Catal.* **1989**, *56*, 9–22. [CrossRef]
178. Sarvaramini, A.; Larachi, F. Catalytic oxygenless steam cracking of syngas-containing benzene model tar compound over natural Fe-bearing silicate minerals. *Fuel* **2012**, *97*, 741–750. [CrossRef]
179. Bian, Z.; Li, Z.; Ashok, J.; Kawi, S. A highly active and stable Ni–Mg phyllosilicate nanotubular catalyst for ultrahigh temperature water-gas shift reaction. *Chem. Commun.* **2015**, *51*, 16324–16326. [CrossRef] [PubMed]
180. Kunkel, T.S.; Krasilin, A.A.; Khrapova, E.K.; Straumal, E.A.; Nomine, A.; Ghanbaja, J.; Ankudinov, A. V Charge injection into the Ni-phyllosilicate nanoscrolls with reduced Ni nanoparticles using Kelvin force probe microscopy. In Proceedings of the IOP Conference Series: Materials Science and Engineering, Ekaterinburg, Russian, 25–28 August 2019; Volume 699, p. 012023. [CrossRef]
181. Zhang, C.; Zhu, W.; Li, S.; Wu, G.; Ma, X.; Wang, X.; Gong, J. Sintering-resistant Ni-based reforming catalysts obtained via the nanoconfinement effect. *Chem. Commun.* **2013**, *49*, 9383. [CrossRef]
182. Bian, Z.; Kawi, S. Preparation, characterization and catalytic application of phyllosilicate: A review. *Catal. Today* **2020**, *339*, 3–23. [CrossRef]

183. Ashok, J.; Ang, M.L.; Terence, P.Z.L.; Kawi, S. Promotion of the Water-Gas-Shift Reaction by Nickel Hydroxyl Species in Partially Reduced Nickel-Containing Phyllosilicate Catalysts. *ChemCatChem* **2016**, *8*, 1308–1318. [CrossRef]
184. Sivaiah, M.V.; Petit, S.; Beaufort, M.F.; Eyidi, D.; Barrault, J.; Batiot-Dupeyrat, C.; Valange, S. Nickel based catalysts derived from hydrothermally synthesized 1:1 and 2:1 phyllosilicates as precursors for carbon dioxide reforming of methane. *Microporous Mesoporous Mater.* **2011**, *140*, 69–80. [CrossRef]
185. Zhang, C.; Yue, H.; Huang, Z.; Li, S.; Wu, G.; Ma, X.; Gong, J. Hydrogen Production via Steam Reforming of Ethanol on Phyllosilicate-Derived Ni/SiO_2: Enhanced Metal–Support Interaction and Catalytic Stability. *ACS Sustain. Chem. Eng.* **2013**, *1*, 161–173. [CrossRef]
186. Bian, Z.; Suryawinata, I.Y.; Kawi, S. Highly carbon resistant multicore-shell catalyst derived from Ni-Mg phyllosilicate nanotubes@silica for dry reforming of methane. *Appl. Catal. B Environ.* **2016**, *195*, 1–8. [CrossRef]
187. Philip, A.; Lihavainen, J.; Keinänen, M.; Pakkanen, T.T. Gold nanoparticle-decorated halloysite nanotubes—Selective catalysts for benzyl alcohol oxidation. *Appl. Clay Sci.* **2017**, *143*, 80–88. [CrossRef]
188. Vinokurov, V.; Stavitskaya, A.; Glotov, A.; Ostudin, A.; Sosna, M.; Gushchin, P.; Darrat, Y.; Lvov, Y. Halloysite nanotube-based cobalt mesocatalysts for hydrogen production from sodium borohydride. *J. Solid State Chem.* **2018**, *268*, 182–189. [CrossRef]
189. Stavitskaya, A.; Mazurova, K.; Kotelev, M.; Eliseev, O.; Gushchin, P.; Glotov, A.; Kazantsev, R.; Vinokurov, V.; Lvov, Y. Ruthenium-Loaded Halloysite Nanotubes as Mesocatalysts for Fischer–Tropsch Synthesis. *Molecules* **2020**, *25*, 1764. [CrossRef]
190. Sadjadi, S.; Lazzara, G.; Heravi, M.M.; Cavallaro, G. Pd supported on magnetic carbon coated halloysite as hydrogenation catalyst: Study of the contribution of carbon layer and magnetization to the catalytic activity. *Appl. Clay Sci.* **2019**, *182*, 105299. [CrossRef]
191. Zhao, Z.; Ren, P.; Li, W. Supported Ni catalyst on a natural halloysite derived silica–alumina composite oxide with unexpected coke-resistant stability for steam-CO_2 dual reforming of methane. *RSC Adv.* **2016**, *6*, 49487–49496. [CrossRef]
192. Zhang, X.; Wang, P.; Wu, X.; Lv, S.; Dai, J. Application of MnO_x/HNTs catalysts in low-temperature NO reduction with NH_3. *Catal. Commun.* **2016**, *83*, 18–21. [CrossRef]
193. Szczepanik, B. Photocatalytic degradation of organic contaminants over clay-TiO_2 nanocomposites: A review. *Appl. Clay Sci.* **2017**, *141*, 227–239. [CrossRef]
194. Abbasov, V.M.; Ibrahimov, H.C.; Mukhtarova, G.S.; Abdullayev, E. Acid treated halloysite clay nanotubes as catalyst supports for fuel production by catalytic hydrocracking of heavy crude oil. *Fuel* **2016**, *184*, 555–558. [CrossRef]
195. Cheng, Z.-L.; Sun, W. Preparation and Solar Light Photocatalytic Activity of N-Doped TiO_2-Loaded Halloysite Nanotubes Nanocomposites. *J. Mater. Eng. Perform.* **2015**, *24*, 4090–4095. [CrossRef]
196. Vinokurov, V.A.; Stavitskaya, A.V.; Ivanov, E.V.; Gushchin, P.A.; Kozlov, D.V.; Kurenkova, A.Y.; Kolinko, P.A.; Kozlova, E.A.; Lvov, Y.M. Halloysite Nanoclay Based CdS Formulations with High Catalytic Activity in Hydrogen Evolution Reaction under Visible Light Irradiation. *ACS Sustain. Chem. Eng.* **2017**, *5*, 11316–11323. [CrossRef]
197. Sarvaramini, A.; Larachi, F. Mössbauer Spectroscopy and Catalytic Reaction Studies of Chrysotile-Catalyzed Steam Reforming of Benzene. *J. Phys. Chem. C* **2011**, *115*, 6841–6848. [CrossRef]
198. Teixeira, A.P.C.; Santos, E.M.; Vieira, A.F.P.; Lago, R.M. Use of chrysotile to produce highly dispersed K-doped MgO catalyst for biodiesel synthesis. *Chem. Eng. J.* **2013**, *232*, 104–110. [CrossRef]
199. Narasimharao, K.; Ali, T.T.; Bawaked, S.; Basahel, S. Effect of Si precursor on structural and catalytic properties of nanosize magnesium silicates. *Appl. Catal. A Gen.* **2014**, *488*, 208–218. [CrossRef]
200. López-Salinas, E.; Toledo-Antonio, J.A.; Manríquez, M.E.; Sánchez-Cantú, M.; Cruz Ramos, I.; Hernández-Cortez, J.G. Synthesis and catalytic activity of chrysotile-type magnesium silicate nanotubes using various silicate sources. *Microporous Mesoporous Mater.* **2019**, *274*, 176–182. [CrossRef]
201. Bonelli, B.; Bottero, I.; Ballarini, N.; Passeri, S.; Cavani, F.; Garrone, E. IR spectroscopic and catalytic characterization of the acidity of imogolite-based systems. *J. Catal.* **2009**, *264*, 15–30. [CrossRef]

202. Ookawa, M. Synthesis and Characterization of Fe-Imogolite as an Oxidation Catalyst. In *Clay Minerals in Nature—Their Characterization, Modification and Application*; Valaskova, M., Martynková, G.S., Eds.; InTech: London, UK, 2012; pp. 239–258. ISBN 978-953-51-0738-5.
203. Krasilin, A.A.; Straumal, E.A.; Yurkova, L.L.; Khrapova, E.K.; Tomkovich, M.V.; Shunina, I.G.; Vasil'eva, L.P.; Lermontov, S.A.; Ivanov, V.K. Sulfated Halloysite Nanoscrolls as Superacid Catalysts for Oligomerization of Hexene-1. *Russ. J. Appl. Chem.* **2019**, *92*, 1251–1257. [CrossRef]

© 2020 by the authors. Licensee MDPI, Basel, Switzerland. This article is an open access article distributed under the terms and conditions of the Creative Commons Attribution (CC BY) license (http://creativecommons.org/licenses/by/4.0/).